Materials Horizons

Review on the growth, properties and applications of self-assembled oxide-metal vertically aligned nanocomposite thin films—Current and Future Perspectives

Journal:	*Materials Horizons*
Manuscript ID	MH-REV-07-2020-001111.R2
Article Type:	Review Article
Date Submitted by the Author:	10-Nov-2020
Complete List of Authors:	Misra, Shikhar; Purdue University Wang, Haiyan; Purdue University System, MSE; Neil Armstrong Engineering Building

SCHOLARONE™
Manuscripts

Review on the growth, properties and applications of self-assembled oxide-metal vertically aligned nanocomposite thin films—Current and Future Perspectives

Shikhar Misra,[a] Haiyan Wang[a,b,*]

[a]School of Materials Engineering, Purdue University, West Lafayette, Indiana 47907, United States
[b]School of Electrical and Computer Engineering, Purdue University, West Lafayette, Indiana 47907, United States

[*]Author to whom correspondence should be addressed. E-mail: hwang00@purdue.edu

Keywords: vertically aligned nanocomposites (VANs), oxide-metal nanocomposite, metamaterials, magnetic materials, hybrid materials

Abstract

Self-assembled oxide-metal nanocomposite thin films have attracted a great research interest owing to their wide range of functionalities, including metamaterials with plasmonic and hyperbolic optical properties, and, ferromagnetic, ferroelectric and multiferroic behaviors. Oxide-metal nanocomposites typically self-assemble as metal particle in oxide matrix or as vertically aligned nanocomposite (VAN) with metal nanopillars embedded in oxide matrix. Among them, the VAN architecture is particularly interesting due to their vertical strain control and highly anisotropic structure enabling the epitaxial growth of materials with large lattice mismatch. In this review, the driving forces behind the formation of the self-assembled oxide-metal VAN structures are discussed. Specifically, an updated in-plane strain compensation model based on areal strain compensation concept has been proposed in this review, based on the prior linear strain compensation model. It provides a guideline on materials selection for designing VAN systems, especially those involving complex orientation matching relationships. Based on the model, several case studies are discussed, comparing the microstructure and morphology of the different oxide-metal nanocomposites by varying the oxide phase. Specific examples highlighting the coupling between the electrical, magnetic and optical properties are also discussed in the context of oxide-metal nanocomposites. Future research directions and needs are also discussed.

1. Introduction

Oxide-metal based composites have attracted significant research interest owing to their unique functionalities and applications in various fields such as catalysis, magnetic data storage, energy storage, and optical metamaterials applications.[1–13] Due to their interesting electrical, magnetic and optical properties, the oxide-metal composites have been vastly explored previously, mostly in the bulk form.[14–20] When reaching to the nanoscale regime, the constituent phases often possess greatly different physical properties from their corresponding bulk counterparts. In addition, for practical applications and easy integration, it is necessary to fabricate these nanocomposites in the form of thin films. Self-assembled nanocomposite thin films offer an interesting approach towards functionality coupling and achieving novel physical properties. Extensive research has been conducted in the field of complex functional oxides and oxide-based nanocomposite thin films, with functionalities ranging from ferromagnetic, ferroelectric, multiferroic, insulating, semiconducting, superconducting, and nonlinear optical effects.[21–32] These functionalities and novel properties arise *via* effective coupling between charge, spin, orbital and lattice degree of freedom.

Recently, oxide-metal hybrid nanostructures have attracted considerable research interest due to their practical device applications such as data storage and optical metamaterials.[1–13] In general, the oxide-metal nanocomposites can be fabricated either by top-down or bottom-up approaches. Figure 1 shows the common fabrication techniques and applications for the oxide-metal nanocomposites. Top-down fabrication techniques include e-beam lithography, nanoimprint lithography and focused ion beam for fabricating and designing oxide-metal nanocomposites.[33–38] For example, nanoimprint lithography can be used to pattern a substrate with sub-10 nm resolution,[39] over a large scale, which can be subsequently coupled with physical vapor deposition (PVD) techniques to fabricate oxide-metal nanocomposites. In addition, bottom-up approaches

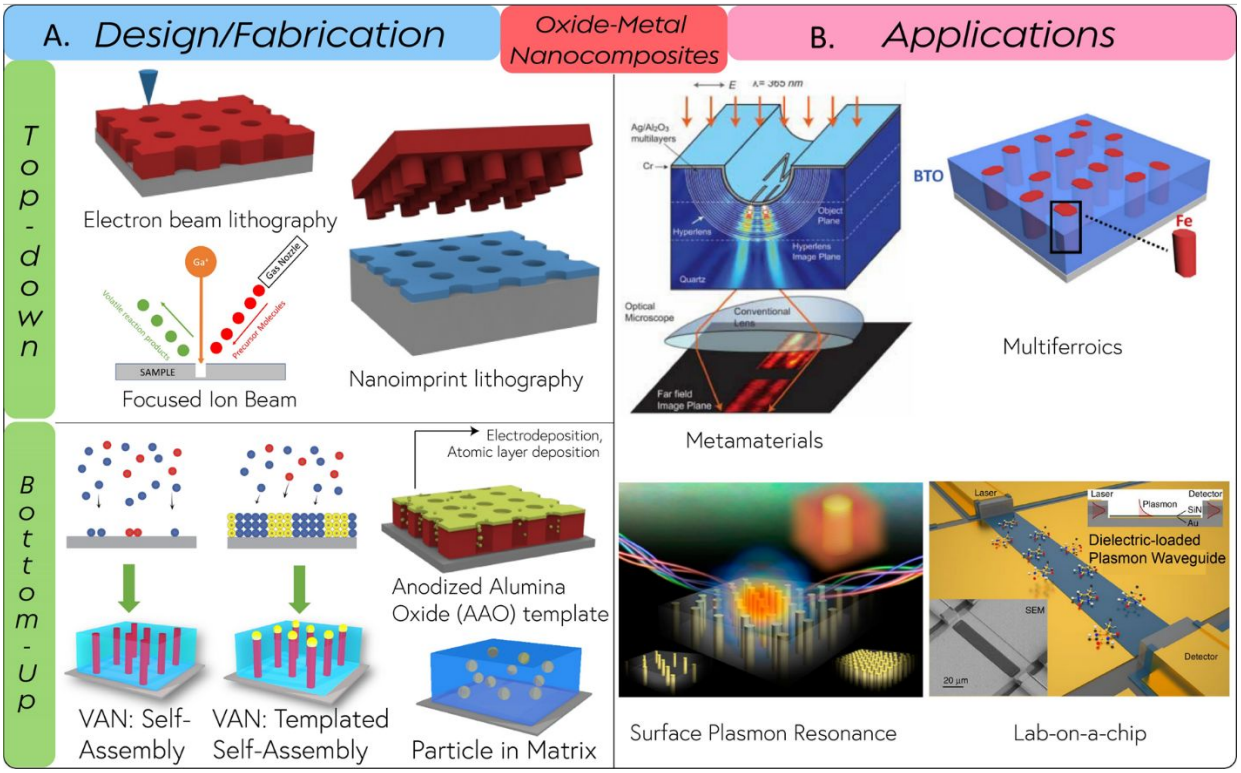

Figure 1. Overview of the oxide-metal nanocomposites. Schematic illustration of the (a) top-down design/fabrication techniques showing the nanoimprint lithography, focused ion beam and electron-beam lithography as labeled, and bottom-up techniques showing the self-assembly, templated self-assembly, particle in matrix and anodized alumina oxide template method. The various applications of the metal-oxide nanocomposites are highlighted in (b). They can be used as metamaterials, multiferroics, plasmonic devices and lab-on-a-chip applications.[40–43] (b) Reproduced with permission from Reference 40, 41, 42, and 43.

such as self-assembly, templated self-assembly and anodized alumina template method can also be used for the growth of oxide-metal nanocomposites.[5,41,44–50] For example, PVD techniques such as Pulsed Laser Deposition (PLD) and sputtering can be used to fabricate a self-assembled oxide-metal nanocomposite as a vertically aligned nanocomposite (VAN) or as a particle in matrix. Different combinations of oxide-metal nanocomposites can find a wide variety of uses ranging from metamaterials, multiferroics, surface enhanced spectroscopy such as fluorescence, Raman

spectroscopy and second harmonic generation to lab-on-a-chip applications, among many others as shown in Figure 1.[41–43,51–59]

Typically, the oxide-metal nanocomposite shows three types of morphology: (i) 0-3 particle-in-matrix (PIM), (ii) 2-2 multilayer, and (iii) 1-3 vertically aligned nanocomposite (VAN). The numbers in front of each of the designs represent the dimensionality of the metallic and oxide phase respectively. The PIM morphology presents a uniform distribution of metallic nanoparticles that are uniformly distributed inside the oxide matrix. The multilayer morphology has the metallic and oxide phases present as alternate layer-by-layer structure; while VANs are self-assembled structures in which both the phases grow epitaxially on the substrate in the out-of-plane direction. Among the 3 different common types of morphologies, lattice coupling at the vertical interface between the two phases and the lateral film/substrate interface play an important role for the growth of VAN thin films which make them particularly interesting due to their highly anisotropic and high interface-to-volume ratio, thereby enabling fascinating physical properties. The vertical strain at the pillar/matrix heterointerface in VAN, provides an extra degree of freedom for tuning the strain and physical properties. The in-plane (IP) strain can be tuned independently from the out-of-plane (OP) strain, with the stiffer phase dominating the final IP and OP state. The growth of VAN thin films offers several advantages. VAN architecture allows the epitaxial growth of materials with high lattice mismatch with the substrate.[9,60–62] Since the two phases are vertically strained, the films can be strained up to a higher thickness as compared to the single-phase thin films in the VAN architecture.[27] In addition, VAN thin films allow easy integration of different functionality, including ferroelectric, ferromagnetic, photocatalytic, superconducting and optical properties. Recently, several VAN systems have been demonstrated in a range of oxide-oxide systems where two different oxides grow as a VAN architecture using a single-step PLD process.

[63–68] For example, systems such as $BaTiO_3$-$CoFe_2O_4$, $BaTiO_3$-Sm_2O_3 and $La_{0.7}Sr_{0.3}MnO_3$ (LSMO)-ZnO have demonstrated room temperature multiferroicity, enhanced ferroelectricity and magnetoresistance respectively.[22,24,27] In comparison, self-assembled oxide-metal nanocomposites offer more opportunities in terms of functionality coupling such as magneto-optical, electro-optic and magneto-electric properties.

However, several challenges arise to achieve self-assembled oxide-metal nanocomposites in epitaxial thin film form, due to the vastly different deposition conditions for oxides and metals. Difference in growth kinetics, surface energy, oxygen diffusion as well as the potential inter-diffusion between the metal and oxides, make it very challenging to achieve epitaxial self-assembled oxide-metal nanocomposites. Very recently, several self-assembled oxide-metal VAN systems have been successfully demonstrated such as Co-$BaZrO_3$, Fe-$BaTiO_3$, Au-$BaTiO_3$, Ni-$Ba(Zr_{0.8}Y_{0.2})O_3$, etc.[41,61,69] Such VAN systems have the capability to couple the electric, magnetic and optical properties and give rise to emergent new properties which are not found in either of the phases. The formation of these self-assembled nanocomposites is driven by a combination of strain and surface energy minimization. Usually, the nanocomposite formation takes place by nucleation and growth during which strain energy play the major role in determining the final morphology during the initial seeding period due to the square dependence on strain as compared to the linear dependence on surface energy.

In this review, we first discuss the two different types of morphology for oxide-metal nanocomposites, deposited using PLD, and differentiate the PIM ones from the VAN ones with some representative examples. In Part I (Sections 2 &3), a newly modified area strain compensation model is proposed for the oxide-metal VANs based on the existing linear strain compensation model developed for the oxide-oxide VANs. These models provide design

guidelines for selecting the two phases and potential IP ordering for VANs. Based on the models, several case studies are discussed to compare the microstructure and morphology of the different oxide-metal VANs by changing the oxide phase. In Part II (Section 4), specific examples highlighting the coupling between the electrical, magnetic and optical properties are discussed of the oxide-metal nanocomposites having both PIM and VAN morphology.

2. Morphology of PIM and VANs and their differences

Oxide-metal nanocomposites typically self-assemble as PIM or as VAN. Usually different crystal structures of metal and oxide gives rise to the nanoparticles-in-matrix type nanocomposite, since it is difficult to maintain the vertical epitaxial relationship between different crystal structures.[1,7,70–73] Figure 2 shows two representative examples of the PIM case. Figure 2a shows the Au-VO_2 nanocomposite (deposited on *c*-cut sapphire substrates) in which Au nanoparticles are uniformly distributed within the VO_2 matrix.[74] Au has a face-centered cubic crystal structure while VO_2 presents a rutile structure at room temperature. VO_2 shows a highly textured growth, corresponding to the (020) plane along the *b* axis while Au NPs show a (111) preferred out-of-plane growth, due to its lowest surface energy, along the OP direction, confirmed using the XRD θ–2θ spectra. The Au NPs show a faceted structure due to the in-plane and out-of-plane lattice coupling with the VO_2 matrix and the lowest packing energy of the (111) plane. The plan-view (i.e. the top-down view) HR-STEM images shown in Figure 2b show the hexagonal lattice structure of Au particles, confirmed by the fast Fourier transform images (inset). Au NPs particles show two major in-plane orientations, given by Au(011)// VO_2(001) and Au(011)//VO_2(100) as determined from the HR-STEM images showing the two types of in-plane matching between Au NPs and VO_2.

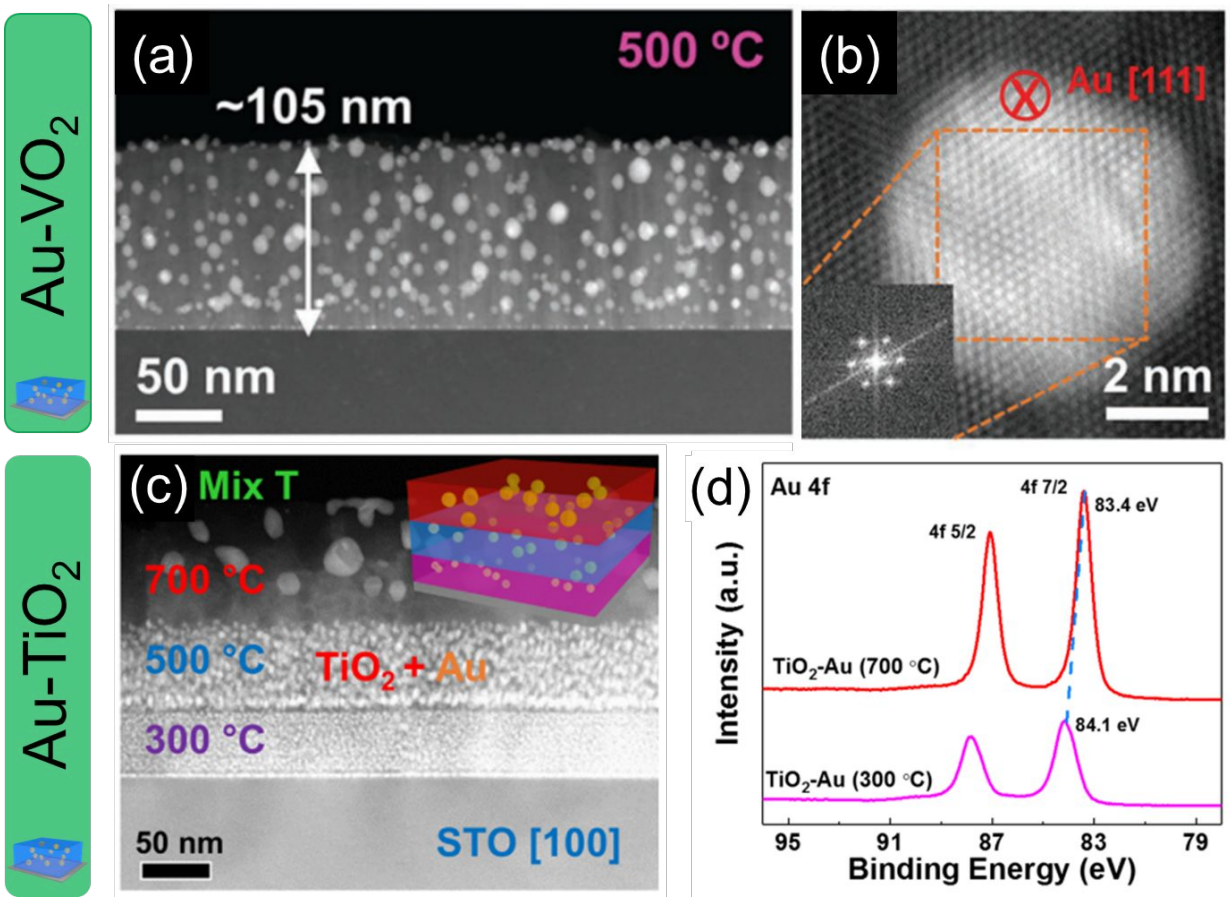

Figure 2. Particle in matrix (PIM) design. (a) Cross-section STEM of the Au-VO_2 nanocomposite thin film deposited on Al_2O_3 (0001) substrate and (b) Plan-view HR-STEM of the Au nanoparticle embedded in VO_2. Inset shows the corresponding FFT patterns. (c) Cross-section STEM image of the multilayer Au-TiO_2 nanocomposite deposited at 300°C, 500°C, and 700°C temperature and (d) XPS spectra of the Au 4f peak.[74,75] Reproduced with permission from Reference 74 and 75.

Another example of the PIM nanocomposite is Au-TiO_2 nanocomposite.[75] TiO_2 grows as an anatase phase, having a tetragonal crystal structure, along the (004) plane in the OP direction while Au grows along the (111) plane. Figure 2c shows the cross-section STEM image of Au-TiO_2 nanocomposite, deposited on $SrTiO_3$ (STO) (001) substrate. It shows the film grown on three different growth temperature: 300°C, 500°C, and 700°C, clearly illustrating the ability to easily tune size and distribution of the Au NPs. The orientation relationship between Au and TiO_2 are determined to be Au(002)//TiO_2(004)//STO(002) and Au(200)// TiO_2(200)//STO(200). The Au

NPs are fully embedded inside and uniformly distributed in the TiO_2 matrix. This makes efficient charge transfer possible from titania to Au NPs as seen from the XPS spectra in Figure 2d, driven by their relative Fermi level energy.[76] The binding energy of Au increases with the decreasing particle size due to the size-dependent electrostatic interaction between the ionized cluster and escaping photoelectron.[77] The distinct advantage of the PIM morphology is the ease of tunability of the metallic NPs shape and size by varying the deposition conditions, which further tunes its physical properties.

Although the growth conditions are similar, the morphology of the nanocomposite can vary from PIM to VAN, depending on the thermodynamic and kinetic factors. For example, using oblique angle deposition (OAD), Au-Li_2MnO_3 nanocomposite can be grown as a VAN morphology but a regular PLD growth leads to a PIM.[78] In addition, several previously reported systems suggest that the large lattice mismatch between the metallic and oxide phase could lead to the PIM growth, while a close lattice matching between the metallic and oxide phases with similar crystal symmetries and epitaxial relationship with the substrate leads to the VAN growth. A representative example of the oxide-metal VAN is Au-$BaTiO_3$ (Au-BTO) shown in Figure 3.[41,79] The Au phase presents as vertical pillars embedded in the BTO matrix (Figure 3b). The X-Ray Diffraction plot in Figure 3a shows the epitaxial growth of BTO on STO along the [001] direction while Au grows primarily along the [001] and [111] direction. The plan-view STEM image (Figure 3c) shows the faceted growth of Au nanopillars and the EDS elemental mapping (Figure 3d) shows no obvious inter-diffusion between the phases. The plan-view HR-STEM micrograph along the BTO <001> zone axis, shown in Figure 3e, shows two twin boundaries from the plan-view HR-STEM image are identified as $[1\bar{1}1]$ and $[11\bar{1}]$, indicating that the Au pillar grows along the [011]

orientation. From the cross-section HR-STEM image in Figure 3f, the Au pillar shows growth along the [002] OP direction. The enlarged image of the Au-BTO vertical interface (Figure 3g)

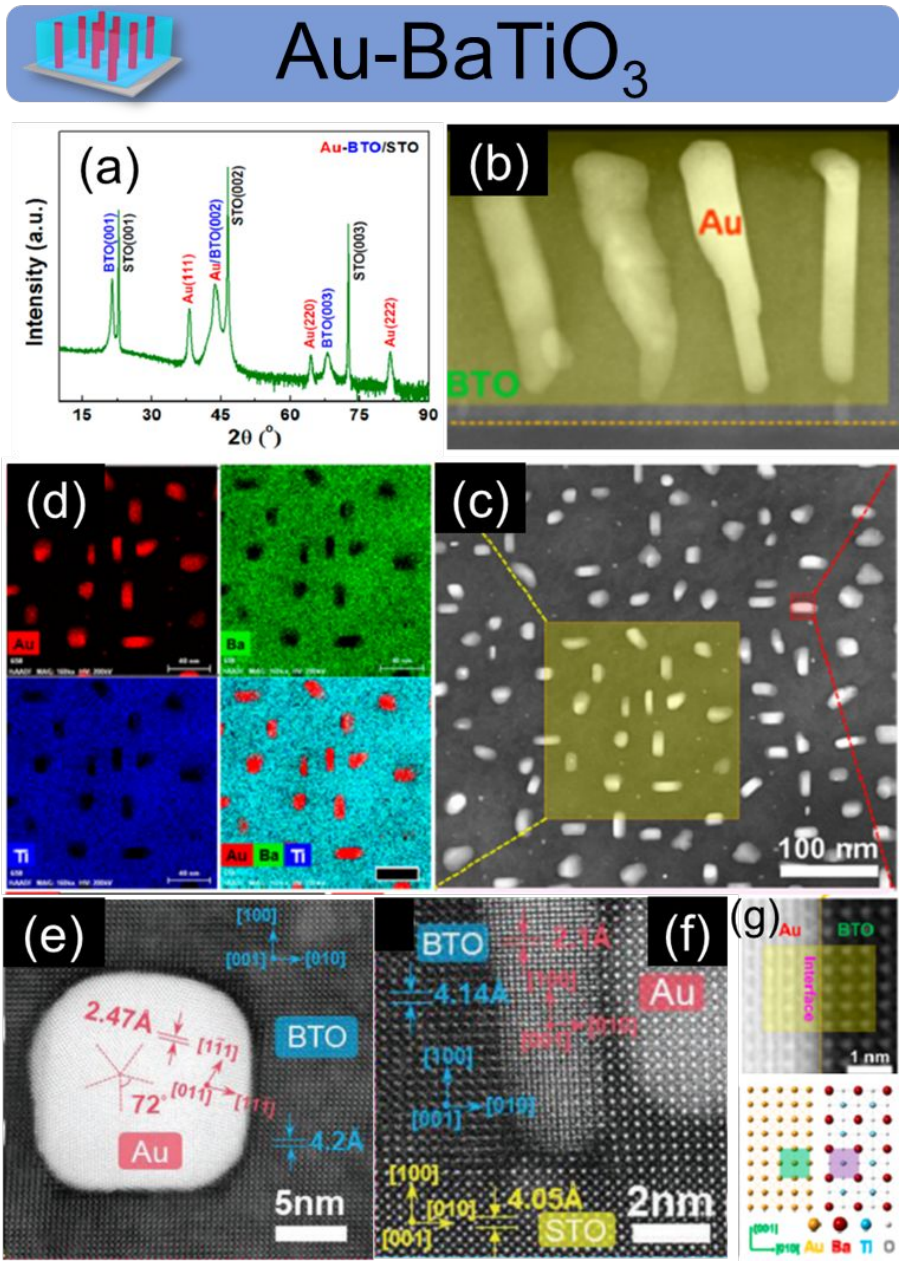

Figure 3. Vertically aligned nanocomposite (VAN) designs. (a) X-ray diffraction of the Au-$BaTiO_3$ nanocomposite, (b) Cross-section, (c) plan-view STEM image and its corresponding (d) EDS elemental map distribution. HR-STEM (e) plan-view image and (f) cross-section image of the Au nanopillar. (g) Enlarged image of the vertical Au-BTO interface and the schematic illustration of the lattice matching relationship.[41,79] Reproduced with permission from Reference 41 and 79.

shows the presence of coherent interface with a 1:1 lattice matching relationship. From the XRD analysis, Au (001), Au (022), and Au (111) are identified as possible growth orientations of the Au pillars. The three matching relationships of the Au-BTO films are given as: BTO(002)‖Au(002)‖STO(002), BTO(002)‖Au(022)‖STO(002), and BTO(002)‖Au(111)‖ STO(002). Further, the Au pillar geometry can be modified by varying the growth parameters such as deposition frequency and laser energy. Therefore, VAN architecture allows the vertical interface coupling between the two phases and maintains the strain in the film up to a much greater thickness as compared to single-phase thin films.

3. Areal strain compensation model vs. linear strain compensation model

As mentioned above, the total IP strain experienced in a VAN structure is given by the sum of the strain from both phases' interfaces with the substrate. The average IP strain experienced by the VAN structure depends on the relative phase composition (i.e. molar or atomic ratio) and their lattice mismatch. A linear strain compensation model has been proposed for the oxide-oxide systems which discussed about the materials selection criteria, based on the lattice parameter, for obtaining an ordered VAN structure.[80] In the cases of the recently reported metal-oxide VAN systems, the nucleation and growth is reported to be the major growth mechanisms[41,60,61,81] with few cases that the metallic phase forms by reducing oxides, such as the Fe nanopillars in LSFO matrix.[82] The specific growth mechanisms for the metal-oxide VANs are still under exploration as new metal-oxide VANs are reported. During the initial nucleation and growth period, strain minimization plays a critical role due to its square dependence in the free energy term as compared to the surface energy minimization which has a linear dependence in the free energy term. Further, the energy difference between the competitive surfaces in different growth orientation is not much

(~within 10-20%) as compared to the strain energy in different growth orientations.[83] Therefore, a growth orientation with a lower strain and higher surface energy is preferred over a growth orientation with a higher strain and a lower surface energy. This linear strain compensation model fits in the oxide-oxide system well as they typically result in a cube-on-cube matching relationship and thus the composition calculation follows a general linear relationship as illustrated in Figure 4b. However, for the oxide-metal case, the orientation of the metal phase could be quite different from the oxide ones and thus an areal based strain compensation model could be more complete. For example, metal in a (111) orientation matching with a (001) oxide, requires areal strain calculation for completeness. However, the 45-degree rotation in oxide-oxide VAN structures is considered as a category of cube on cube epitaxy matching. Therefore, the linear strain compensation can be applied in such cases by considering a matching distance of $a/\sqrt{2}$. Both the linear and areal strain compensation models have been built using the published VAN data. However, the model needs to be updated based on other factors such as dislocation formation at the interface. Below both the linear and areal strain compensation models are discussed and compared with case studies presented.

3.1 Linear strain compensation model

Figure 4a shows the schematic of the lattice matching relationship between the metal and oxide phases with the substrate. The IP lattice mismatch strain is calculated using:

$$f = 2\frac{a_f - a_s}{a_f + a_s}$$

where a_f and a_s are lattice parameter of the film and the substrate, respectively. The model calculates the lattice mismatch along one dimension and works best for the cases when there is a cube on cube epitaxy with no rotation, with lattice parameters being equal in both the IP directions.

Since the total IP strain in the nanocomposite depends on the phase composition, Figure 4b plots the metal and oxide lattice parameter (on the left and right vertical axis) as a function of phase composition (on the X-axis) using the rule of mixtures with the STO substrate marked by a solid black line of the reported oxide-metal VAN systems.[3,9,12,13,41,60–62,82,84–89] Clearly the trendlines of all the reported VAN structures indicate the minimization of the effective IP strain as experienced by the nanocomposite. The lattice parameters of the metal and oxide phases are plotted in Figure 4c. The plot can be divided into two regions based on the strain compensation. Region I (shaded in orange) is defined as the space where both the tensile and compressive strain acts on the two phases while region II (shaded in blue) defines the space where either compressive or tensile strain acts on both the phases. Further, several systems are marked (with a red star), indicating a highly spatially ordered VAN structure. Region I result in effective strain compensate on and contains majority of the reported VAN structures. However, when one of the phases undergoes a rotation or has a different crystal structure than the substrate, it results in different lattice parameter matching in the *a* and *b* directions, and linear strain model can only model one of the directions. In order to overcome this limitation, the aerial strain compensation model is proposed.

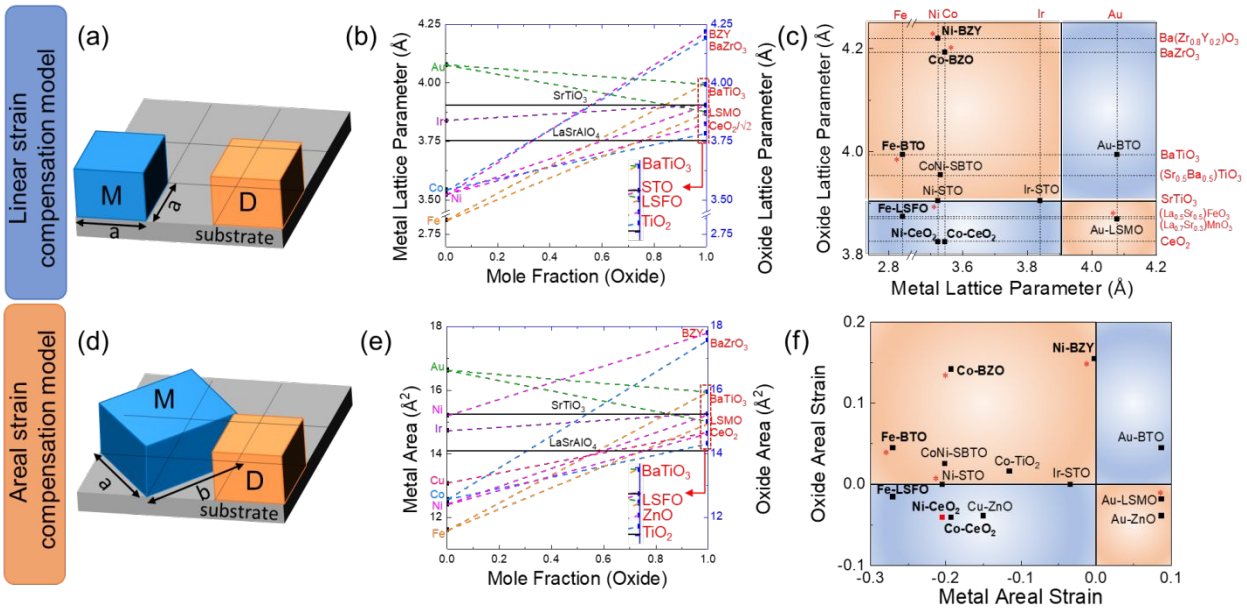

Figure 4. Linear and Areal strain compensation models. Schematic illustration of lattice matching relationship for the (a) linear and (d) areal strain compensation model. (b) In-plane lattice constant and (e) area for the metal and oxide phases as a function of oxide mole fraction. The dashed line joining the metal and oxide phases are the reported VAN systems and indicate the tunability of the in-plane strain on the substrate. Substrate are marked with a solid black line. (c) Plot showing the reported metal-oxide VAN systems plotted with their lattice parameters and (f) areal strain. The orange portions represent the region where both tensile and compressive strain is present while the blue shaded portion represent the region where either both tensile or compressive strain is present. The VAN systems marked with red star indicate highly spatially ordered systems.

3.2 Areal strain compensation model

The areal strain compensation model considers the two-dimensional lattice matching between the phases and the substrate. As shown in Figure 4d, when one of the phases undergoes a rotation or has a different crystal structure, then strain is calculated using the projected area onto the substrate considering the IP matching between the phase and the substrate. The strain is calculated using:

$$f = 2\frac{A_f - A_s}{A_f + A_s}$$

where A_f and A_s are the matching area of film and substrate, respectively. Area is calculated using the appropriate lattice matching relationship. For example, if the metallic phase is cubic and the oxide phase is hexagonal as in the case of Cu-ZnO, then it becomes hard to calculate the strain using the linear model since Cu and ZnO grows along [001] and $[11\bar{2}0]$ on STO [001] along the OP direction. Cu shows a cube-on-cube epitaxy on STO substrate while ZnO has different lattice parameters along the *a* and *b* directions as shown schematically in Figure 4c. The oxide strain can be calculated by comparing the oxide area with the corresponding substrate area. Similarly, matching in other orientations can also be calculated. In the case of cube-on-cube epitaxy relationships, the linear strain model and the areal strain model gives the same result however, the areal strain model provides an advantage when the epitaxy relationship occurs between different crystal structures.

Figure 4e plots the areal lattice parameter for both the metal and oxide phases as a function of oxide mole fraction. Clearly, it is seen that all the trendlines work on minimizing the overall IP areal strain. Interestingly, the IP area strain of Ni (in Ni-Ba($Zr_{0.8}Y_{0.2}$)O_3 (BZY) system) is calculated to be almost 0, compared to the non-zero strain calculated in the linear model, which is discussed in much more detail in the case studies in the following section. Figure 4f presents the reported oxide-metal VAN systems, plotted as a function of metal and oxide areal strain. Similar to the linear strain compensation model the plot can be divided into 2 regimes depending on the strain nature, i.e, tensile or compressive strain. We observe that most of the highly ordered VAN structure (marked with a red star) present in regime I where there is effective strain compensation. Based on these observations, the formation of self-assembled ordered VAN structures can be attributed to several key factors: (i) a close lattice match between the two phases and the substrate,

(ii) presence of opposite strain nature, i.e., the structures are present in regime I, (iii) Similar crystal structures of the two phases, and (iv) low solubility of the two phases.

The following section presents three case studies of the VAN structures, for which the nanocomposite systems have been reported in both regime I and regime II, having the same metallic phase but different oxide phase. The VAN systems selected for comparison are marked in Figure 4f.

3.3 Case Studies

As discussed earlier, when the metallic and oxide phases experience opposite strain, i.e., tensile strain in one phase and compressive strain in the other phase (region I), they present more ordered VAN structure as compared to those cases that both the phases experience strain of the same sign, i.e., both tensile or compressive strain. Figure 5 compares the microstructure of Co-CeO_2 and Co-$BaZrO_3$ (BZO), both deposited on STO (001) substrate using PLD.[13,61,85] Co and CeO_2 experiences a compressive strain while BZO experience a tensile strain. Co crystallizes as either FCC or HCP structure while both CeO_2 and BZO have a cubic structure. In the case of Co-CeO_2 nanocomposite Co NWs are not perfectly aligned in the growth direction of [001] as seen in Figure 5a. The structure analyses using the HR-STEM further reveals that the misalignment is due to the HCP structure of Co NWs with their hexagonal *c* axis aligned along the <111> axis of the matrix as confirmed by Figure 5c1 and 5c3. Although in some minor portions of the NWs, Co is present as a cubic structure (Figure 5c2). In contrast, Co-BZO shows primarily the FCC Co structure with growth along the [002] and [022] direction as confirmed by the plan-view HR-STEM image in Figure 5e. The cross-section HR-STEM image in Figure 5f-g shows the lattice matching relationship along the vertical interface between Co and BZO, with calculated *d* spacing of 1.82 Å and 2.12 Å for $d_{Co\ (002)}$ and $d_{BZO\ (002)}$, respectively, showing the possibility of domain

matching epitaxy and suggesting the presence of tensile strain in Co pillars Although the Co pillar diameter is almost similar in both the systems (~5 nm), Co pillars present a more spatially ordered structure in BZO, with more aligned and continuous pillars. Therefore, effective strain compensation gives rise to a more continuous and ordered structure.

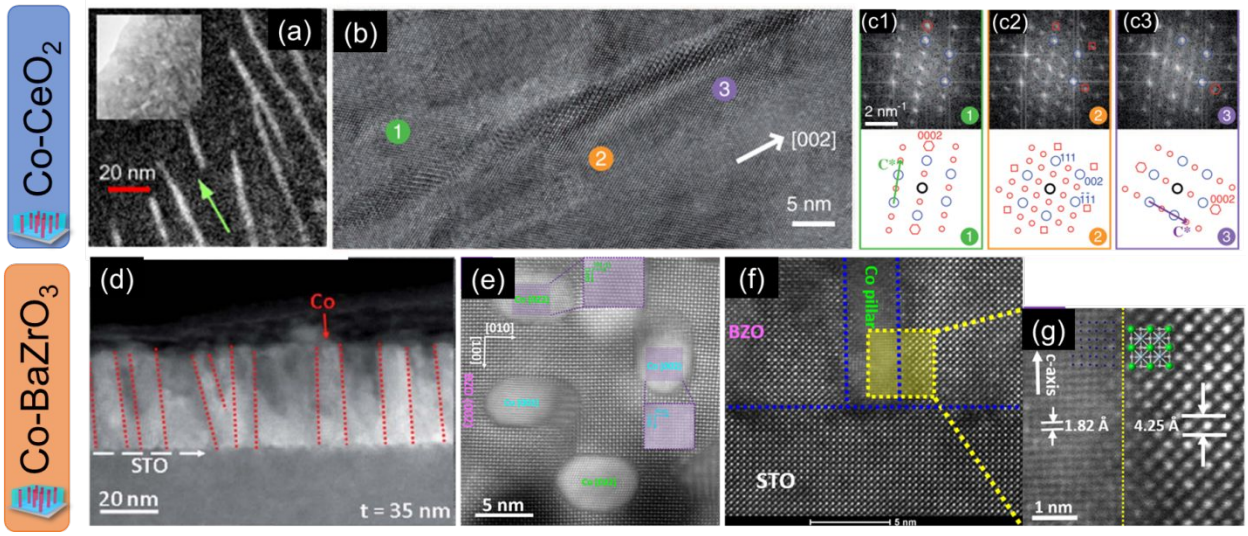

Figure 5. Case study I. (a) Cross-section EF-TEM image of the Co-CeO_2 showing the Co nanowires. (b) HR-TEM image of a Co nanowire and (c1)-(c3) the corresponding SAED patterns of the three regions marked in (b). (d) Cross-section STEM image of Co-$BaZrO_3$ nanocomposite. (e) HR-STEM plan-view image and (f) cross-section image. (g) shows an enlarged portion of the vertical in-terface between Co and $BaZrO_3$.[13,61,85] (a) Reproduced with permission from Reference 13, 61, and 85.

Figure 6 compares the microstructure of Ni-CeO_2 and Ni-BZY, deposited on STO (001) substrate.[60,62] Ni, CeO_2 and BZY have a cubic crystal structure, with Ni and CeO_2 experiencing a compressive strain and BZY having a tensile strain, placing the Ni-CeO_2 in regime II and Ni-BZY system in regime I. The XRD and HR-STEM analysis in Figure 6a-d indicate a cube-on-cube epitaxy of CeO_2 and Ni with both growing in the [001] OP direction. CeO_2 (a_{CeO2}=5.41 Å) undergoes a 45° rotation to match with STO. Ni (a_{Ni}=3.52 Å) preferably grows along the [002] direction with some minor growth along the [022] direction, due to the low surface energy of the

(002) orientation. IP domain matching epitaxy occurs between Ni and STO with $10a_{Ni} \approx 9a_{STO}$. The vertical strain is minimized by the domain matching epitaxy between CeO_2 and Ni since $2a_{CeO2} \approx 3a_{Ni}$. However, Ni grows along the [111] OP direction in BZY matrix with lattice matching relationship given by Ni (011)//BZY (200) and Ni (110)//BZY (110), evidenced by the XRD and HR-STEM plan view images in Figure 6e-h. By maintaining such a relationship, Ni reduces its IP areal strain almost completely to 0, as shown in Figure 4d. In addition to the lowest surface energy of the Ni (111) orientation, the OP *d*-spacing ($d_{Ni(111)}$=2.04 Å) is closely matched with the *d*-spacing of BZY ($d_{BZY(002)}$=2.11 Å) orientation. Therefore, the difference in the growth orientation of Ni can be attributed to the combination of both OP and IP strain minimization. The average Ni pillar diameter increases from ~4 nm (in Ni-BZY) to ~7 nm (in Ni-CeO_2) and the cross-section STEM image shows a clear difference in the Ni pillar morphology. The Ni pillars are non-continuous and non-uniform in CeO_2 as compared to the almost vertically aligned pillars and spatially ordered pillars in the BZY matrix.

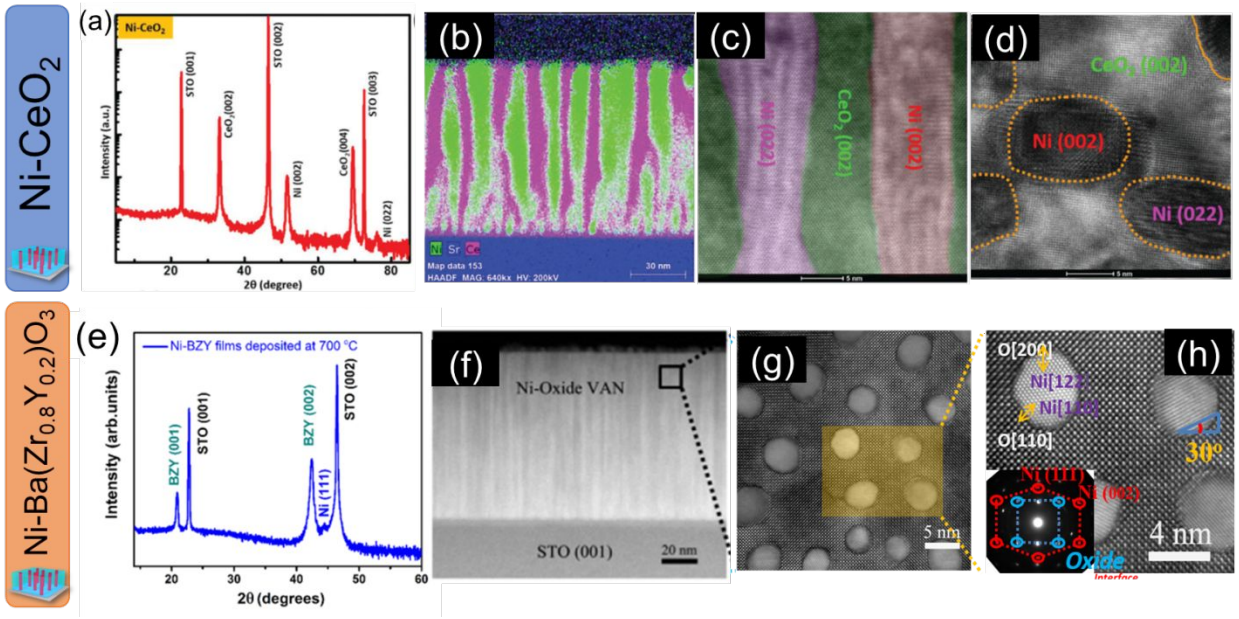

Figure 6. Case study II. X-ray diffraction of Ni-CeO_2 nanocomposite thin film, (b) Cross-section STEM-EDS map showing the elemental distribution, (c) HR-STEM cross-section image and (d) plan-view image showing the two different growth orientation of the Ni pillars. (e) X-ray diffraction of the Ni-$Ba(Zr_{0.8}Y_{0.2})O_3$ (BZY) nanocomposite thin film, (f) Cross-section STEM image, (g) Plan-view STEM image and (h) the corresponding HR-STEM image showing the Ni growth orientation.[60,62] Reproduced with permission from Reference 60 and 62.

The last case study compares the Fe pillar structure embedded in $(La_{0.5}Sr_{0.5})FeO_3$ (LSFO) and BTO, deposited on STO (001) substrate.[82,90] Fe and BTO crystallizes as a cubic structure while LSFO has tetragonal crystal structure. LSFO and Fe have a compressive strain while BTO has a tensile strain on the STO substrate. XRD plot in Figure 7a and 7e shows the epitaxial growth of LSFO and BTO in the [001] direction. Although the Fe phase grows in the [110] OP direction, the morphology of the embedded Fe pillars shows much difference. Fe pillar diameter decreases from ~15 nm in LSFO to ~5 nm in BTO. Further, the microstructure changes from a less-ordered particle-like growth to a more ordered pillar-type growth. Such a change in microstructure can be attributed to the effective strain compensation along the lateral and vertical interfaces between Fe and the oxide matrix. Moreover, changing the growth parameters such as the laser frequency and

laser energy also tunes the size of the Fe pillars. Therefore, judicious selection of the metallic and the oxide phases, based on the strain compensation model, offers enormous opportunities for tuning the microstructure of the oxide-metal nanocomposites.

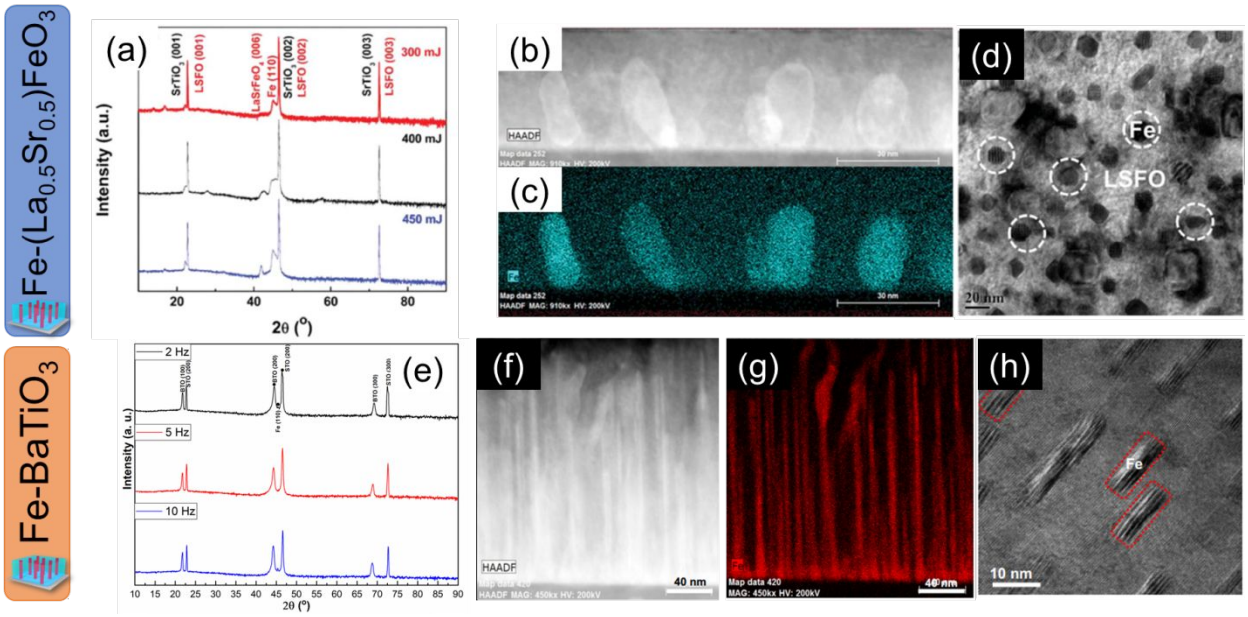

Figure 7. Case study III. X-ray diffraction of the Fe-$(La_{0.5}Sr_{0.5})FeO_3$ (LSFO) nanocomposite thin film deposited with different laser energy. (b) Cross-section STEM image and (c) the corresponding Fe EDS map. (d) Plan-view TEM image showing the distribution of Fe pillars. (e) X-ray diffraction of the Fe-$BaTiO_3$ nanocomposite thin film deposited at different laser frequency. (f) Cross-section STEM image and (g) the corresponding Fe EDS map. (d) Plan-view TEM image showing the faceted structure of Fe pillars.[82,90] Reproduced with permission from Reference 82 and 90.

Taking advantages of the opposite strain in some of the oxide-metal VANs and their nicely VAN morphologies, one can use it as a buffer layer to grow other complex systems and couple physical properties, including ferroelectricity, ferromagnetism and exotic optical properties. As an example, a self-assembled ordered three-phase Au-BTO-ZnO nanocomposite was successfully demonstrated as shown in Figure 8 by using BTO-Au as the buffer layer.[5] Both BTO and ZnO grow epitaxially on STO (001) substrate while Au grows primarily along the [111] OP direction.

The cross-section STEM-EDS shows a mix of Au particles, capping the ZnO nanowires, as well as Au pillars, embedded in the BTO matrix (Figure 8b-d). In addition, the plan-view STEM-EDS mapping shows the ordered growth of both ZnO and Au phases. Such unique microstructure is achieved by a two-step template assisted growth. First, Au-BTO VAN is deposited which acts as a template for the subsequent BTO-ZnO VAN growth. Since, BTO is present in both the layers, ZnO preferentially gets deposited on top of Au pillars. Interestingly, Au and ZnO form a low melting point eutectic solution, which gives rise to the ZnO nanowires upon becoming supersaturated with ZnO. This mechanism is called the Vapor-Liquid-Solid (VLS) mechanism. Therefore, the 'nanoman'-like structure is enabled by the combination of template-assisted VLS and two-phase epitaxy growth mechanisms. Such multi-phase structure opens new possibilities in design, growth and engineering of other systems towards increased control over light-electron-matter interaction at the nanoscale.

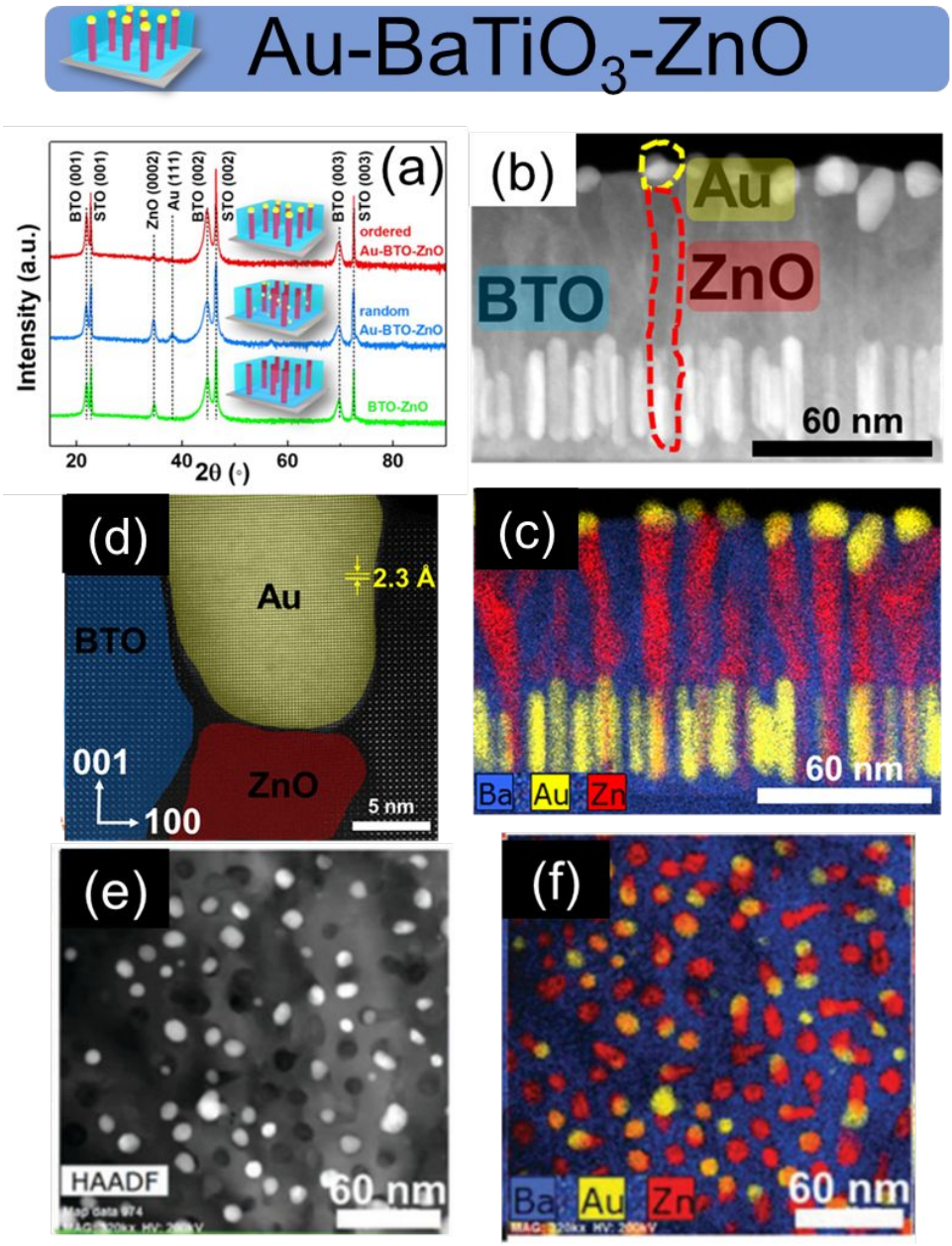

Figure 8. Three-phase nanocomposite. (a) Comparison of the X-ray diffraction of the two-phase $BaTiO_3$-ZnO, random three-phase Au-$BaTiO_3$-ZnO and ordered three-phase Au-$BaTiO_3$-ZnO nanocomposite thin films, (b) Cross-section STEM image and (c) the corresponding EDS elemental map of the Au-$BaTiO_3$-ZnO nanocomposite, (d) HR-STEM image showing the interface between Au, $BaTiO_3$ and ZnO, (e) Plan-view STEM image and (f) the corresponding EDS elemental map of the Au-$BaTiO_3$-ZnO nanocomposite thin film.[5] Reproduced with permission from Reference 5.

4. Functionality

Oxide-metal nanocomposites enable a wide range of novel functionality by coupling the properties of metals and oxides. By combining appropriate oxides and metals, it is possible to couple electrical, magnetic and optical properties as illustrated in Figure 9. The Heckmann diagram helps to understand the coupling between the external stimuli, such as electric field (E) and magnetic field (H), with the associated materials properties such as oxide polarization (P_d), electronic polarization (P_e) and magnetization (M). The corresponding coupling coefficients are described by electric susceptibility (χ_e), optical susceptibility (χ_o), and magnetic susceptibility (χ_h), respectively. The coupled materials effects can be visualized using this Heckmann diagram. The three ends of the Heckmann diagram have been previously explored in self-assembled oxide-oxide based nanocomposite and have only been recently focused in the self-assembled oxide-metal nanocomposites. The choice of metal offers greater flexibility in terms of nanocomposite design for the functionality coupling. For example, a plasmonic metallic pillar in a ferroelectric matrix can be used to enhance the non-linearity of the ferroelectric, described by the electro-optic effects. Similarly, magneto-electric effects and magneto-optic effects can be achieved through coupled materials properties.[91–94] Taking as a recent example, strong magneto-optic coupling via MOKE measurements has been demonstrated in Fe-Au-BTO VAN systems.[95] The electro-optic coupling coefficient haven't been directly measured as indicated by a faded line in the Heckmann diagram. The following section gives specific examples of nanocomposites that have been used to explore the application space as described by the Heckmann diagram.

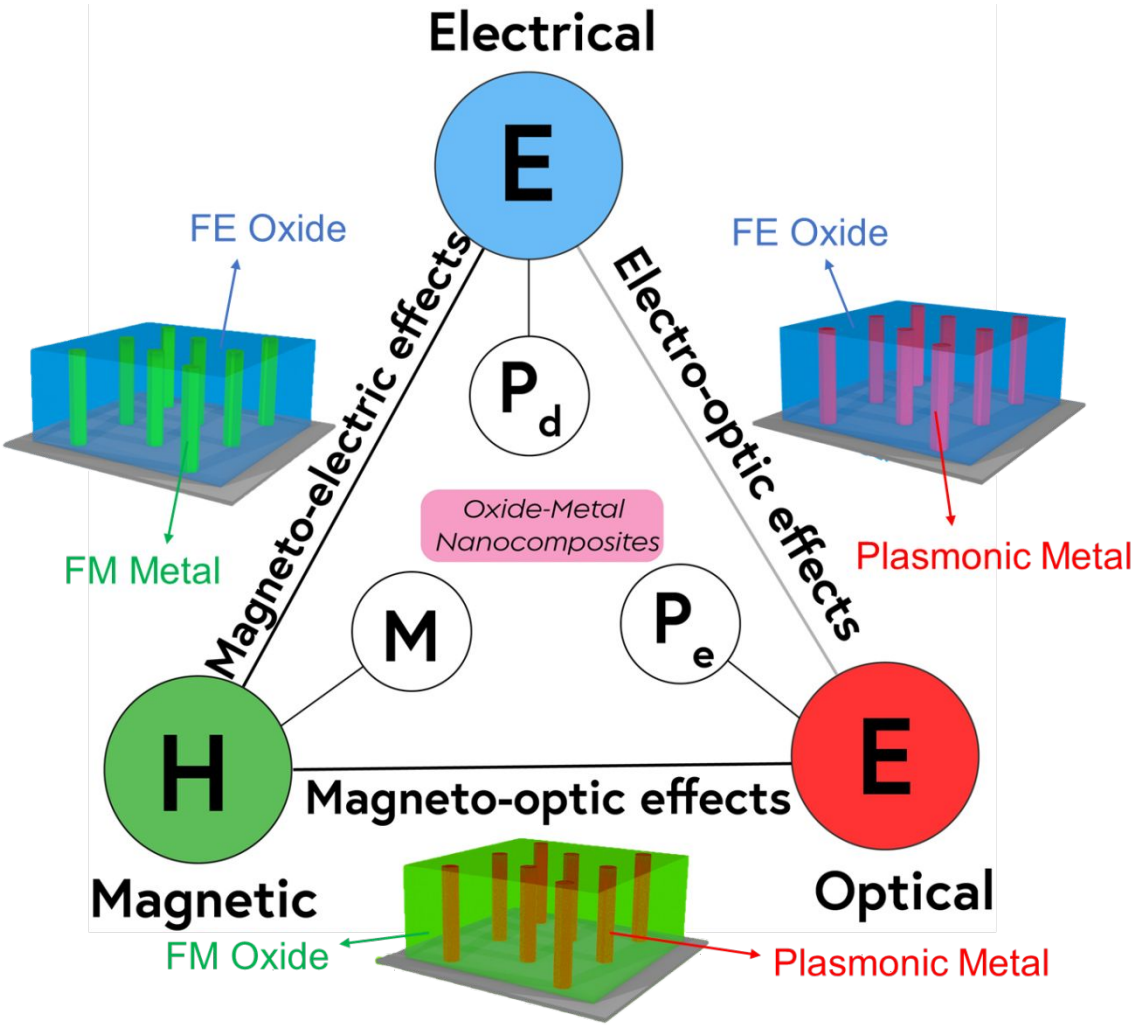

Figure 9. Heckmann diagram showing the multifunctionalities and coupling effects of the VAN structures

Figure 10 presents the optical end of the Heckmann diagram, showing the morphology, optical property and specific functionality for three different nanocomposites: Au-BTO, Au-BTO-ZnO and Au-$LiNbO_3$ (Au-LNO).[5,8,41] All the three nanocomposites consist of plasmonic metal and a ferroelectric oxide as the metallic and oxide phases, respectively. Self-assembled two-phase Au-BTO and three-phase Au-BTO-ZnO show VAN architecture as discussed earlier while Au-LNO show a PIM morphology. All the three systems show surface plasmon resonance in the visible wavelength regime due to presence of Au, resulting in an increased absorbance. The plasmonic

absorption peak shifts systematically, depending on the size of the Au pillar and NP. In addition, due to the highly anisotropic and ordered structure of Au-BTO VAN, its OP permittivity becomes negative in the near-infrared (NIR) wavelength regime while maintaining the positive IP permittivity (shown in Figure 10a3). Due to this inherent anisotropic permittivity, the nanocomposite behaves as a 'metal' in one direction and as a 'dielectric' in the other direction. Such functionality is described by the hyperbolic dispersion of the wavevectors, supporting the propagation of very high wavevectors through this hybrid material. Therefore, Au-BTO behaves as a hyperbolic metamaterial in the NIR wavelength regime. Interestingly, the presence of both Au pillars and particles, capping the ZnO nanowires, in the three-phase Au-BTO-ZnO, makes the 'nanoman'-like structure hyperbolic even in the visible wavelength regime. Such metamaterials can be used in range of exciting applications such as nanolithography, sub-diffraction imaging, and optical sensing the visible and NIR wavelength. Lastly, Au-LNO hybrid nanocomposite has been demonstrated as a tunable waveguide, being integrated on silicon, enabled by the vastly different refractive index of Si (n_{Si}=3.3) and Au-LNO ($n_{Au\text{-}LNO}$=2.23). The incorporation of Au NPs also enhances the non-linearity of LNO as evidenced by the increased second-harmonic generation (SHG) signal due to increased number of Au and LNO non-linear interfaces. Therefore, the plasmonic metal-dielectric hybrid materials offer interesting capabilities towards photonics device integration.

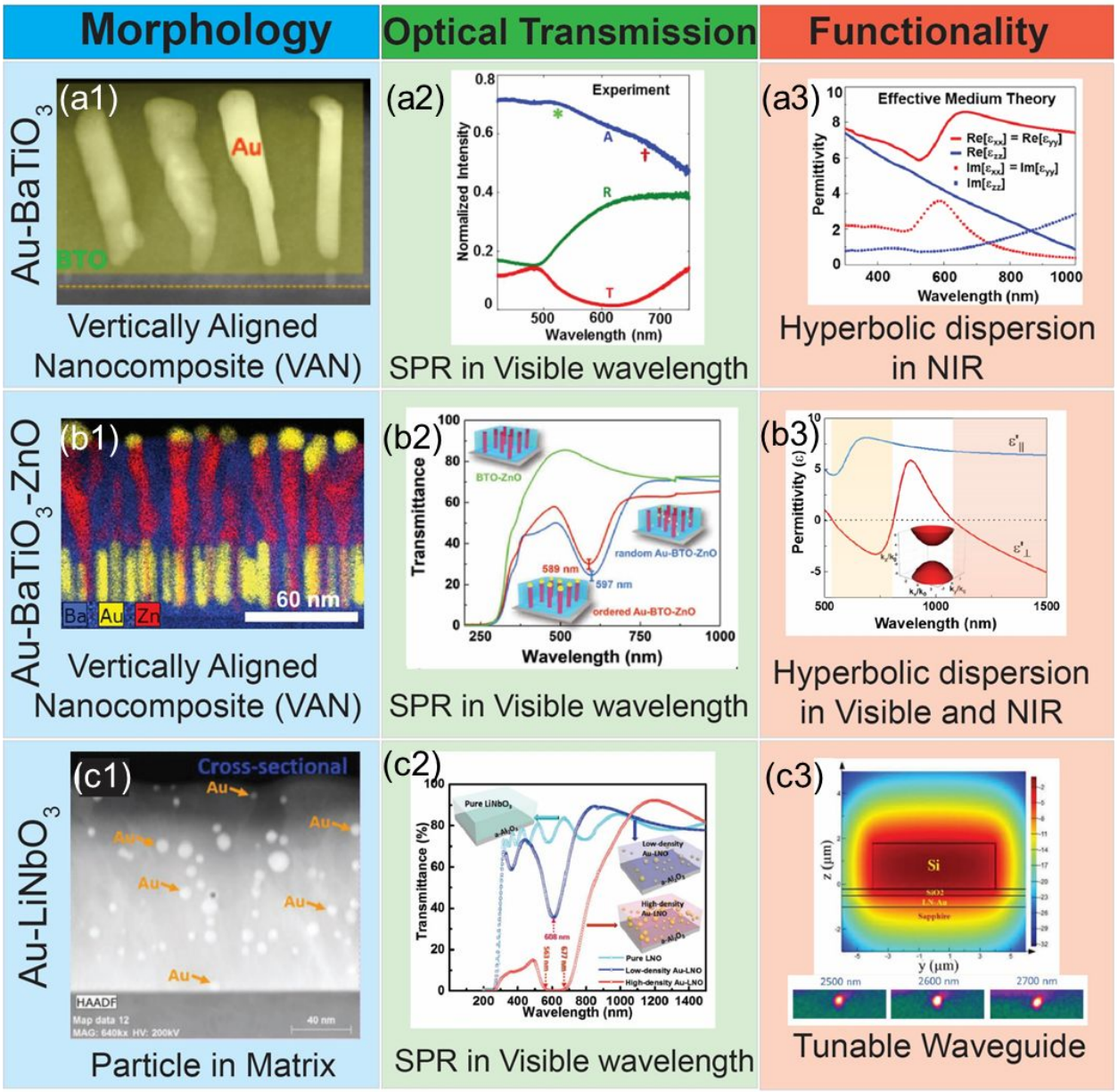

Figure 10. Optical functionalities. Morphology, optical transmission and the specific functionality of (a1-a3) Au-$BaTiO_3$, (b1-b3) Au-$BaTiO_3$-ZnO, and (c1-c3) Au-$LiNbO_3$ nanocomposite thin films.[5,8,41] Reproduced with permission from Reference 5, 8, and 41.

Figure 11 presents the magnetic end of the Heckmann diagram, where the metallic phase is a ferromagnetic metal. Three different nanocomposite systems are shown: Ni-BZY, Co-BZO, and

Fe-BTO, all having VAN structure.[61,62,88] The magnetization panel compares the IP and OP magnetic hysteresis loops for the three systems. Typically, both structure anisotropy and

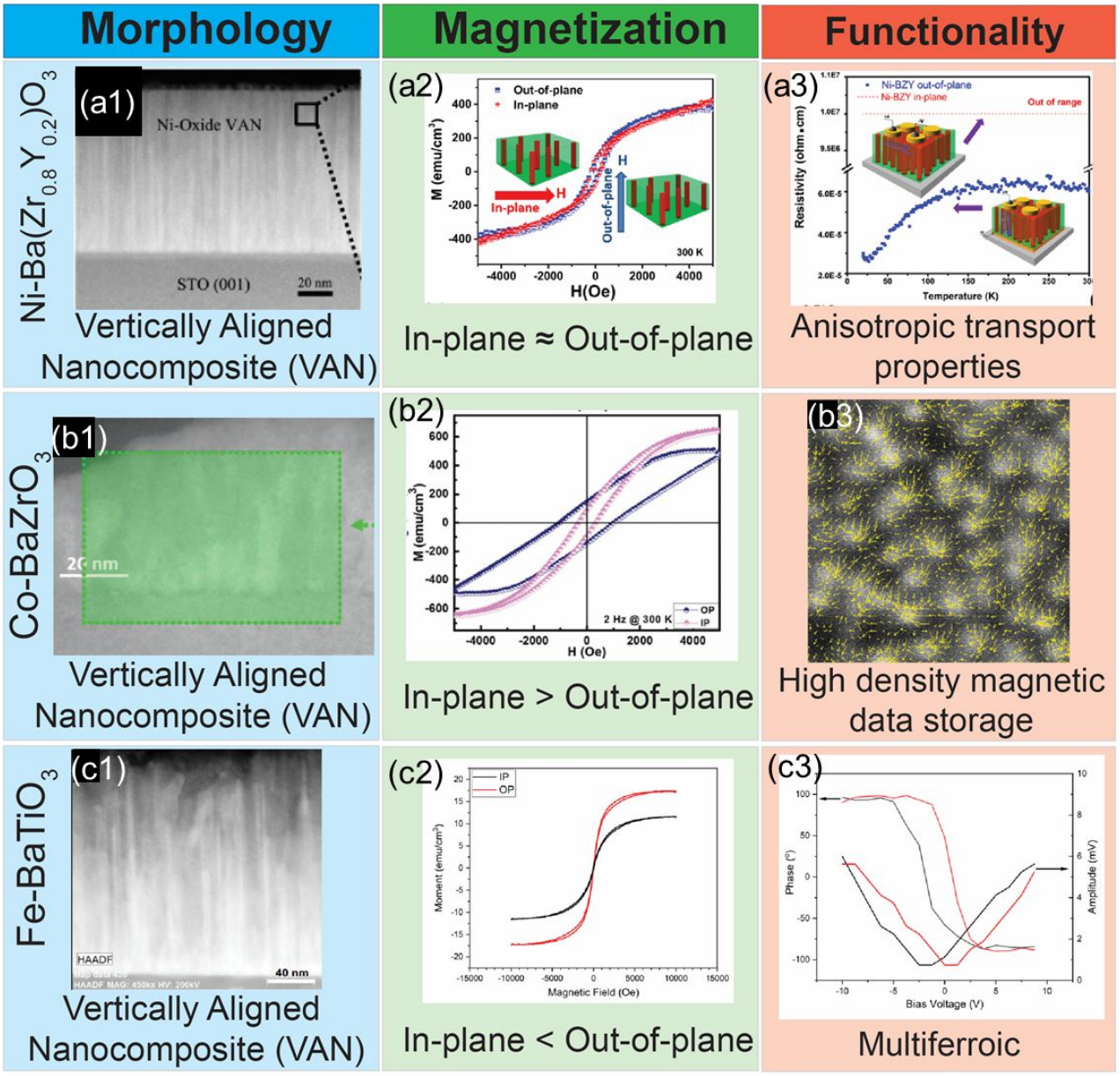

Figure 11. Magnetic functionalities. Morphology, magnetization hysteresis and the specific functionality of (a1-a3) Ni-Ba($Zr_{0.8}Y_{0.2}$)O_3 (BZY), (b1-b3) Co-$BaZrO_3$ (BZO), and (c1-c3) Fe-$BaTiO_3$ (BTO) nanocomposite thin films. [61,62,88] Reproduced with permission from Reference 61, 62, and 88.

magnetocrystalline anisotropy determine the anisotropic magnetization. Using a judicious materials selection, the IP and OP magnetization anisotropy can be appropriately tuned to have either stronger IP or OP magnetization as compared in Figure 11a2, 11b2, and 11c2. The inherent anisotropic structure of Ni-BZY gives rise to vastly different transport properties in the lateral and vertical direction as seen in Figure 11a3. The OP resistivity is low ranging from 2.5 to 6 Ohm cm due to presence of the metallic phase while the IP resistivity is extremely high due to the highly insulating BZY matrix. Such anisotropic transport properties can enable novel thermoelectric materials. The metal- oxide nanocomposite with a metallic ferromagnetic phase can be used in high density magnetic storage as seen by the IP magnetization texture of Co-BZO (Figure 11b3). The length and direction of the vectors represent the magnitude and orientation of the magnetization vector. These hybrid materials can be used in perpendicular recording media. Further, if the oxide is ferroelectric, then the nanocomposite can couple both the ferroic properties, resulting in a multiferroic material as shown by Fe-BTO (Figure 11c3). The Fe-BTO VAN exhibits both magnetic and polarization hysteresis loops, as well as the magneto-electric coupling making it a candidate for the multiferroic material.

Figure 12 shows the nanocomposite systems near the electrical property end of the Heckmann diagram. Three different nanocomposite systems: Au-VO_2, Au-TiO_2 and Au-Li_2MnO_3 (Au-LMO) are presented.[4,74,78] As discussed earlier, Au-VO_2 and Au-TiO_2 show PIM morphology while Au pillars exist as tilted pillars in LMO matrix, deposited using oblique-angle PLD. The presence of the Au metallic phase helps tune the bandgap of the overall nanocomposite which further gets tuned based on the size of Au NP as seen in the tunability panel of Figure 12. For example, varying the deposition temperature from 600°C to 350°C, decreases the Au NP diameter from ~12nm to ~2nm in the case of Au-VO_2 nanocomposite. Such a decrease in Au NP diameter

increases the bandgap from ~1.7 eV to ~2.1 eV. In addition, it also decreases the phase transition temperature of VO_2 from 348K to 323.5K, thereby effectively tuning the phase change property. Similarly, decrease in the Au NP diameter upon decreasing the deposition temperature results in the reduction in the bandgap in Au-TiO_2 nanocomposite, which enhances the overall photocatalytic activity. Further, the presence of tilted Au pillars in LMO matrix have shown to enhance the electrochemical performance of the thin film cathode (Figure 12c3). Such hybrid materials can find potential application in electrochromics, sensors, actuators, efficient photocatalysts, and in thin film batteries. In most of these systems, the electrical, magnetic and optical properties are measured independently and it's challenging to directly measure the coupling coefficients between them. Therefore, more work needs to be done to explore these coupling effects in other nanocomposites. Thus, a careful selection of the metallic and oxide phase in the metal- oxide nanocomposite presents enormous opportunities for realizing next generation integrated electronic, magnetic and photonic devices.

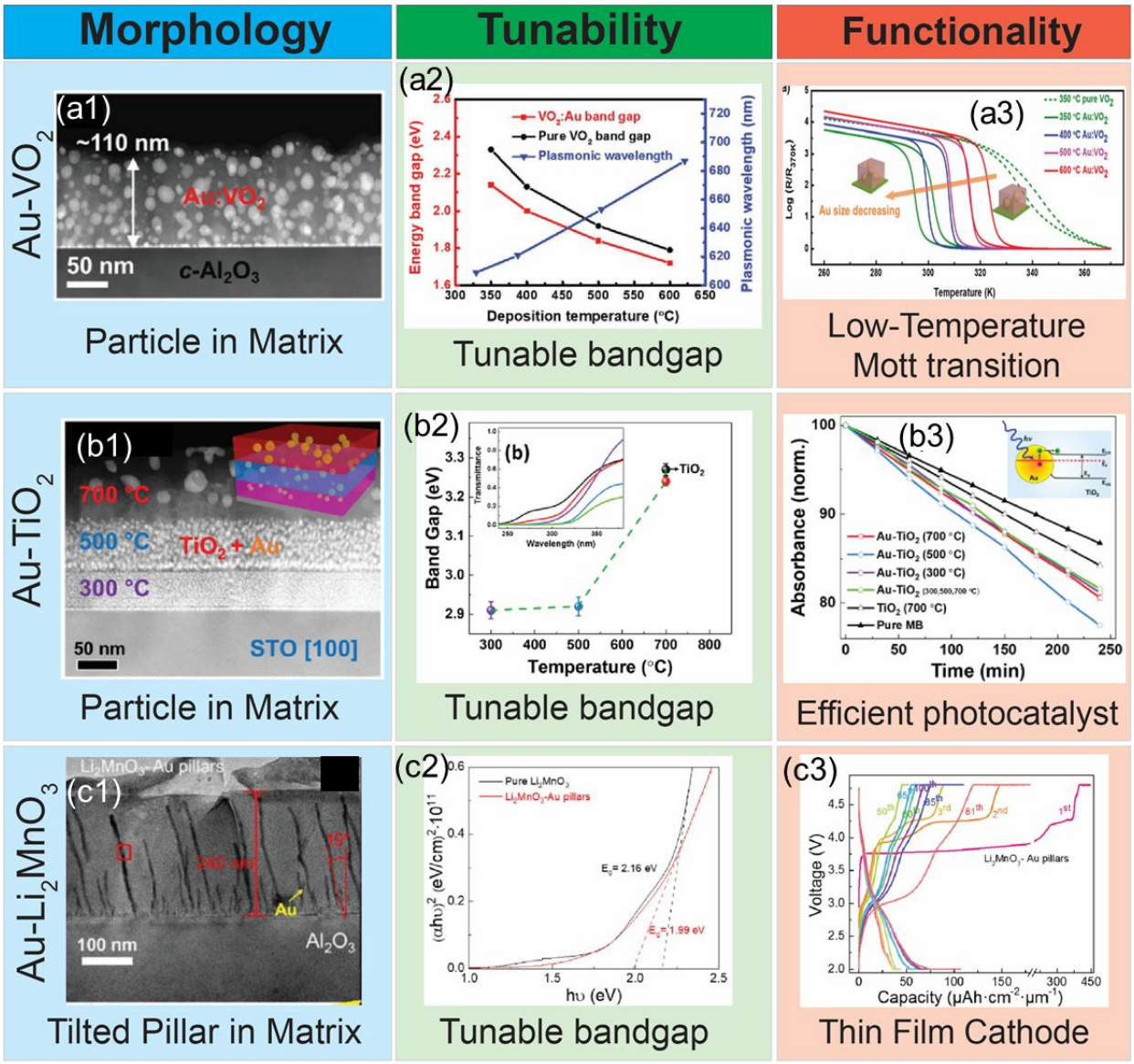

Figure 12. Electrical functionalities. Morphology, tunable bandgap and the specific functionality of (a1-a3) Au-VO_2, (b1-b3) Au-TiO_2, and (c1-c3) Au-Li_2MnO_3 nanocomposite thin films. [4,74,78] Reproduced with permission from Reference 4, 74, and 78.

5. Summary and Outlook

This review has summarized the recent progress in the self-assembled oxide-metal nanocomposites, their design criteria and their functionalities. Overall, oxide-metal nanocomposites offer unique advantages over oxide-oxide nanocomposites in terms of new functionalities and tunable microstructure. The nanoparticle size can be easily tuned in the PIM

design while the VAN architecture allows flexible tunability of the pillar dimensions. Effective strain compensation is the driving force behind the formation of highly spatially ordered VAN structure. Novel combined functionalities and anisotropic properties have been demonstrated, including ferroelectric, ferromagnetic and plasmonic properties covering all corners of the Heckmann diagram.

Regarding the future research directions, there are enormous amount of new oxide-metal nanocomposite candidates with novel functionalities to be explored. Some of the selected focused areas are: (1) Owing to the large possibilities of materials combinations, various oxide-metal VAN systems are yet to be explored that can enable different multifunctionalities. Figure 4 provides a guideline on materials selection for designing VAN systems based on the IP strain compensation. Highly spatially ordered structures can be achieved by careful materials selection which provide an important building block for metamaterial application. However, domain matching epitaxy should also be considered while exploring potential VAN systems. (2) Most of the nanocomposite thin film systems have been reported on specific oriented single crystal substrates such as STO (001), $LaAlO_3$ (LAO) (001), Sapphire (0001), MgO (001) etc. Since these substrates are small and expensive, they are not ideal for scaling up and device integration. Therefore, interesting and potential systems should be grown on Si substrates or flexible substrates such as Mica with the aim of achieving device integration and novel properties with few recent success in oxide-metal nanocomposites, which can be integrated in Si-based devices or flexible electronics.[96] (3) Further work is needed in the exploration of three-phase nanocomposite for achieving greater design flexibility. Materials selection can be done by examining the bulk ternary, quaternary, or pseudo-binary phase diagrams for potential eutectic points or alloy formation.

Acknowledgements

This work was supported by the U.S. Department of Energy, Office of Science, Basic Energy Sciences under Award DE-SC0020077. This paper describes objective technical results and analysis. Any subjective views or opinions that might be expressed in the paper do not necessarily represent the views of the U.S. Department of Energy or the United States Government. S.M. acknowledges the Purdue Bilsland Dissertation Fellowship support and the partial support from the Office of Naval Research N00014-20-1-2600.

References

1. K. Au, X. S. Gao, J. Wang, Z. Y. Bao, J. M. Liu, and J. Y. Dai: Enhanced resistive switching effect in Ag nanoparticle embedded BaTiO 3 thin films. *J. Appl. Phys.* **114**, 027019 (2013).
2. N. Fang, H. Lee, C. Sun, and X. Zhang: Sub–Diffraction-Limited Optical Imaging with a Silver Superlens. *Science (80-.).* **308**, 534 (2005).
3. V. Schuler, F. J. Bonilla, D. Demaille, A. Coati, A. Vlad, Y. Garreau, M. Sauvage-Simkin, A. Novikova, E. Fonda, S. Hidki, V. Etgens, F. Vidal, and Y. Zheng: Huge metastable axial strain in ultrathin heteroepitaxial vertically aligned nanowires. *Nano Res.* **8**(6), 1964 (2015).
4. S. Misra, L. Li, J. Jian, J. Huang, X. Wang, D. Zemlyanov, J.-W. Jang, F. H. Ribeiro, and H. Wang: Tailorable Au Nanoparticles Embedded in Epitaxial TiO2 Thin Films for Tunable Optical Properties. *ACS Appl. Mater. Interfaces* **10**, 32895 (2018).
5. S. Misra, L. Li, D. Zhang, J. Jian, Z. Qi, M. Fan, H. Chen, X. Zhang, and H. Wang: Self-Assembled Ordered Three-Phase Au – BaTiO 3 – ZnO Vertically Aligned Nanocomposites Achieved by a Templating Method. *Adv. Mater.* **31**(7), 1806529 (2018).

6. I. Fasaki, M. Kandyla, and M. Kompitsas: Properties of pulsed laser deposited nanocomposite NiO:Au thin films for gas sensing applications. *Appl. Phys. A Mater. Sci. Process.* **107**(4), 899 (2012).

7. I. Fasaki, M. Kandyla, M. G. Tsoutsouva, and M. Kompitsas: Optimized hydrogen sensing properties of nanocomposite NiO:Au thin films grown by dual pulsed laser deposition. *Sensors Actuators, B Chem.* **176**, 103 (2013).

8. J. Huang, T. Jin, S. Misra, H. Wang, Z. Qi, Y. Dai, X. Sun, L. Li, J. Okkema, H. Chen, P. Lin, X. Zhang, and H. Wang: Tailorable Optical Response of Au – LiNbO3 Hybrid Metamaterial Thin Films for Optical Waveguide Applications. *Adv. Opt. Mater.* No. 1800510, 1 (2018).

9. J. Huang, X. Wang, X. L. Phuah, P. Lu, Z. Qi, and H. Wang: Plasmonic Cu nanostructures in ZnO as hyperbolic metamaterial thin films. *Mater. Today Nano* **8**, 100052 (2019).

10. S. Kawasaki, R. Takahashi, T. Yamamoto, M. Kobayashi, H. Kumigashira, J. Yoshinobu, F. Komori, A. Kudo, and M. Lippmaa: Photoelectrochemical water splitting enhanced by self-assembled metal nanopillars embedded in an oxide semiconductor photoelectrode. *Nat. Commun.* **7**, 11818 (2016).

11. R. L. Paldi, X. Sun, X. Wang, X. Zhang, and H. Wang: Strain-Driven In-plane Ordering in Vertically Aligned ZnO–Au Nanocomposites with Highly Correlated Metamaterial Properties. *ACS Omega* **5**, 2234 (2020).

12. V. Schuler, J. Milano, A. Coati, A. Vlad, M. Sauvage-Simkin, Y. Garreau, D. Demaille, S. Hidki, A. Novikova, E. Fonda, Y. Zheng, and F. Vidal: Growth and magnetic properties of vertically aligned epitaxial CoNi nanowires in (Sr, Ba)TiO3 with diameters in the 1.8-6 nm range. *Nanotechnology* **27**, 495601 (2016).

13. P. Schio, F. Vidal, Y. Zheng, J. Milano, E. Fonda, D. Demaille, B. Vodungbo, J. Varalda, A. J. A. De Oliveira, and V. H. Etgens: Magnetic response of cobalt nanowires with diameter below 5 nm. *Phys. Rev. B - Condens. Matter Mater. Phys.* **82**(9), 094436 (2010).

14. X. Li, W. Qi, D. Mei, M. L. Sushko, I. Aksay, and J. Liu: Functionalized graphene sheets as molecular templates for controlled nucleation and self-assembly of metal oxide-graphene nanocomposites. *Adv. Mater.* **24**(37), 5136 (2012).

15. W. P. Chen, Y. Xiong, Y. S. Li, P. Cui, S. S. Guo, W. Chen, Z. L. Tang, Z. Yan, and Z. Zhang: Extraordinary room-temperature hydrogen sensing capabilities of porous bulk Pt-TiO2 nanocomposite ceramics. *Int. J. Hydrogen Energy* **41**(4), 3307 (2016).

16. B. J. Clapsaddle, D. W. Sprehn, A. E. Gash, J. H. Satcher, and R. L. Simpson: A versatile sol-gel synthesis route to metal-silicon mixed oxide nanocomposites that contain metal oxides as the major phase. *J. Non. Cryst. Solids* **350**, 173 (2004).

17. T. Liu, B. Li, Y. Hao, F. Han, L. Zhang, and L. Hu: A general method to diverse silver/mesoporous-metal-oxide nanocomposites with plasmon-enhanced photocatalytic activity. *Appl. Catal. B Environ.* **165**, 378 (2015).

18. P. D. Cozzoli, R. Comparelli, E. Fanizza, M. L. Curri, A. Agostiano, and D. Laub: Photocatalytic Synthesis of Silver Nanoparticles Stabilized by TiO 2 Nanorods: A Semiconductor/Metal Nanocomposite in Homogeneous Nonpolar Solution. *J. Am. Chem. Soc.* **126**(12), 3868 (2004).

19. D. Wang, D. Cai, C. Wang, B. Liu, L. Wang, Y. Liu, H. Li, Y. Wang, Q. Li, and T. Wang: Muti-component nanocomposite of nickel and manganese oxides with enhanced stability and catalytic performance for non-enzymatic glucose sensors. *Nanotechnology* **27**(25) (2016).

20. A. Tanaka, A. Ogino, M. Iwaki, K. Hashimoto, A. Ohnuma, F. Amano, B. Ohtani, and H. Kominami: Gold-titanium(IV) oxide plasmonic photocatalysts prepared by a colloid-photodeposition method: Correlation between physical properties and photocatalytic activities. *Langmuir* **28**(36), 13105 (2012).

21. A. Chen, H. Zhou, Z. Bi, Y. Zhu, Z. Luo, A. Bayraktaroglu, J. Phillips, E. Choi, J. L. Macmanus-driscoll, S. J. Pennycook, J. Narayan, Q. Jia, X. Zhang, and H. Wang: A New Class of Room-Temperature Multiferroic Thin Films with Bismuth-Based Supercell Structure. *Adv. Mater.* **25**, 1028 (2013).

22. A. Chen, W. Zhang, F. Khatkatay, Q. Su, C. F. Tsai, L. Chen, Q. X. Jia, J. L. Macmanus-Driscoll, and H. Wang: Magnetotransport properties of quasi-one-dimensionally channeled vertically aligned heteroepitaxial nanomazes. *Appl. Phys. Lett.* **102**(9), 093114 (2013).

23. X. Sun, J. Huang, J. Jian, M. Fan, H. Wang, Q. Li, J. L. Macmanus-Driscoll, P. Lu, X. Zhang, and H. Wang: Three-dimensional strain engineering in epitaxial vertically aligned nanocomposite thin films with tunable magnetotransport properties. *Mater. Horizons* **5**, 536 (2018).

24. H. Zheng, J. Wang, S. E. Lofland, Z. Ma, T. Zhao, S. R. Shinde, S. B. Ogale, F. Bai, D. Viehland, Y. Jia, D. G. Schlom, M. Wuttig, A. Roytburd, and R. Ramesh: Multiferroic BaTiO3 -CoFe2O4 Nanostructures. *Science (80-.).* **303**, 661 (2004).

25. S. Cho, J. Jang, L. Li, J. Jian, H. Wang, and J. L. Macmanus-driscoll: Self-Assembled Heteroepitaxial Oxide Nanocomposite for Photoelectrochemical Solar Water Oxidation. *Chem. Mater.* **28**, 3017 (2016).

26. M. Fan, B. Zhang, H. Wang, J. Jian, X. Sun, J. Huang, L. Li, X. Zhang, and H. Wang: Self-Organized Epitaxial Vertically Aligned Nanocomposites with Long-Range Ordering

Enabled by Substrate Nanotemplating. *Adv. Mater.* 1 (2017).

27. S. A. Harrington, J. Zhai, S. Denev, V. Gopalan, H. Wang, Z. Bi, S. A. T. Redfern, S. Baek, C. W. Bark, C. Eom, Q. Jia, M. E. Vickers, and J. L. Macmanus-driscoll: Thick lead-free ferroelectric films with high Curie temperatures through nanocomposite- induced strain. *Nat. Nanotechnol.* **6**(July), 491 (2011).

28. J. Jian, X. Wang, L. Li, M. Fan, W. Zhang, J. Huang, Z. Qi, and H. Wang: Continuous Tuning of Phase Transition Temperature in VO 2 Thin Films on c - Cut Sapphire Substrates via Strain Variation. *ACS Appl. Mater. Interfaces* **9**, 5319 (2017).

29. J. Kim, Y. Kim, Y. S. Kim, J. L. Kim, D. Jung, J. Kim, Y. Kim, Y. S. Kim, and J. Lee: Large nonlinear dielectric properties of artificial superlattices Large nonlinear dielectric properties of artificial BaTiO3/SrTiO3 superlattices. *Appl. Phys. Lett.* **80**, 3581 (2002).

30. L. Li, P. Boullay, J. Cheng, P. Lu, X. Wang, G. Steciuk, J. Huang, J. Jian, X. Gao, B. Zhang, S. Misra, X. Zhang, K. Yang, and H. Wang: Self-assembled two-dimensional layered oxide supercells with modulated layer stacking and tunable physical properties. *Mater. Today Nano* **6**, 100037 (2019).

31. L. Li, P. Boullay, P. Lu, X. Wang, J. Jian, J. Huang, X. Gao, S. Misra, W. Zhang, O. Perez, G. Steciuk, A. Chen, X. Zhang, and H. Wang: Novel Layered Supercell Structure from Bi2AlMnO6 for Multifunctionalities. *Nano Lett.* **17**(11), 6575 (2017).

32. S. Misra, L. Li, X. Gao, J. Jian, Z. Qi, D. Zemlyanov, and H. Wang: Tunable physical properties in BiAl1-xMnxO3 thin films with novel layered supercell structures. *Nanoscale Adv.* **2**, 315 (2020).

33. M. Kahl, E. Voges, S. Kostrewa, C. Viets, and W. Hill: Periodically structured metallic substrates for SERS. *Sensors Actuators, B Chem.* **51**(1–3), 285 (1998).

34. M. Song and K. Furuya: Fabrication and characterization of nanostructures on insulator substrates by electron-beam-induced deposition. *Sci. Technol. Adv. Mater.* **9**(2), 023002 (2008).

35. Z. J. Zhao, S. H. Hwang, S. Jeon, B. Hwang, J. Y. Jung, J. Lee, S. H. Park, and J. H. Jeong: Three-dimensional plasmonic Ag/TiO2 nanocomposite architectures on flexible substrates for visible-light photocatalytic activity. *Sci. Rep.* **7**(1), 8915 (2017).

36. A. Revaux, G. Dantelle, D. Decanini, A. M. Haghiri-Gosnet, T. Gacoin, and J. P. Boilot: Synthesis of YAG:Ce/TiO2 nanocomposite films. *Opt. Mater. (Amst).* **33**(7), 1124 (2011).

37. D. Wang, R. Kou, D. Choi, Z. Yang, Z. Nie, J. Li, L. V. Saraf, D. Hu, J. Zhang, G. L. Graff, J. Liu, M. A. Pope, and I. A. Aksay: Ternary self-assembly of ordered metal oxide-graphene nanocomposites for electrochemical energy storage. *ACS Nano* **4**(3), 1587 (2010).

38. J. F. Lin, J. P. Bird, L. Rotkina, and P. A. Bennett: Classical and quantum transport in focused-ion-beam-deposited Pt nanointerconnects. *Appl. Phys. Lett.* **82**(5), 802 (2003).

39. S. Y. Chou and P. R. Krauss: Imprint lithography with sub-10 nm feature size and high throughput. *Microelectron. Eng.* **35**(1–4), 237 (1997).

40. B. Zhang, J. Huang, B. X. Rutherford, P. Lu, S. Misra, M. Kalaswad, Z. He, X. Gao, X. Sun, L. Li, and H. Wang: Tunable, Room Temperature Multiferroic Fe-BaTiO3 Vertically Aligned Nanocomposite with Perpendicular Magnetic Anisotropy. *Mater. Today Nano* **11**, 100083 (2020).

41. L. Li, L. Sun, J. S. Gomez-Diaz, N. L. Hogan, P. Lu, F. Khatkhatay, W. Zhang, J. Jian, J. Huang, Q. Su, M. Fan, C. Jacob, J. Li, X. Zhang, Q. Jia, M. Sheldon, A. Alù, X. Li, and H. Wang: Self-assembled epitaxial Au-oxide vertically aligned nanocomposites for nanoscale metamaterials. *Nano Lett.* **16**(6), 3936 (2016).

42. Z. Liu, H. Lee, Y. Xiong, C. Sun, and X. Zhang: Far-Field Optical Hyperlens Magnifying. *Science (80-.).* **315**, 1686 (2007).

43. B. Schwarz, P. Reininger, D. Ristanić, H. Detz, A. M. Andrews, W. Schrenk, and G. Strasser: Monolithically integrated mid-infrared lab-on-a-chip using plasmonics and quantum cascade structures. *Nat. Commun.* **5**, 4085 (2014).

44. M. Lee, S. Hong, and D. Kim: Chemical-free synthesis of electrically connected gold nanotubes/ nanoparticles from solution-infiltrated anodized aluminum oxide template. *Appl. Phys. Lett.* **89**(4), 043120 (2006).

45. L. Wen, R. Xu, Y. Mi, and Y. Lei: Multiple nanostructures based on anodized aluminium oxide templates. *Nat. Nanotechnol.* **12**(3), 244 (2017).

46. J. Huang, L. Li, P. Lu, Z. Qi, X. Sun, X. Zhang, and H. Wang: Self-assembled Co-BaZrO3 nanocomposite thin films with ultra-fine vertically aligned Co nanopillars. *Nanoscale* **9**(23), 7970 (2017).

47. J. Zhang, Z. Fan, Y. Q. Wang, and B. L. Zhou: Equilibrium pseudobinary Al - Mg2Si phase diagram. *Mater. Sci. Technol.* **17**(5), 494 (2001).

48. X. Wang, X. Ma, E. Shi, P. Lu, L. Dou, X. Zhang, and H. Wang: Large-Scale Plasmonic Hybrid Framework with Built-In Nanohole Array as Multifunctional Optical Sensing Platforms. *Small* **1906459**, 1 (2020).

49. X. Wang, J. Jian, Z. Zhou, C. Fan, Y. Dai, L. Li, J. Huang, J. Sun, A. Donohue, P. Bermel, X. Zhang, H.-T. Chen, and H. Wang: Self-Assembled Ag-TiN Hybrid Plasmonic Metamaterial: Tailorable Tilted Nanopillar and Optical Properties. *Adv. Opt. Mater.* **7**(3) (2019).

50. J. Huang, X. Wang, N. L. Hogan, S. Wu, P. Lu, Z. Fan, Y. Dai, B. Zeng, R. Starko-bowes,

J. Jian, H. Wang, L. Li, R. P. Prasankumar, D. Yarotski, M. Sheldon, H. Chen, Z. Jacob, X. Zhang, and H. Wang: Nanoscale Artificial Plasmonic Lattice in Self-Assembled Vertically Aligned Nitride – Metal Hybrid Metamaterials. *Adv. Sci.* **5**, 1800416 (2018).

51. T. Liebermann and W. Knoll: Surface-plasmon field-enhanced fluorescence spectroscopy. *Colloids Surfaces A Physicochem. Eng. Asp.* **171**(1–3), 115 (2000).
52. M. Fiebig, T. Lottermoser, D. Meier, and M. Trassin: The evolution of multiferroics. *Nat. Rev. Mater.* **1**(8) (2016).
53. R. F. Aroca: Plasmon enhanced spectroscopy. *Phys. Chem. Chem. Phys.* **15**(15), 5355 (2013).
54. S. K. Gray: Surface plasmon-enhanced spectroscopy and photochemistry. *Plasmonics* **2**(3), 143 (2007).
55. L. Baldassarre, E. Sakat, J. Frigerio, A. Samarelli, K. Gallacher, E. Calandrini, G. Isella, D. J. Paul, M. Ortolani, and P. Biagioni: Midinfrared Plasmon-Enhanced Spectroscopy with Germanium Antennas on Silicon Substrates. *Nano Lett.* **15**(11), 7225 (2015).
56. C. L. Haynes and R. P. Van Duyne: Plasmon-sampled surface-enhanced Raman excitation spectroscopy. *J. Phys. Chem. B* **107**(30), 7426 (2003).
57. Y. Zhang, K. Aslan, M. J. R. Previte, and C. D. Geddes: Metal-enhanced fluorescence: Surface plasmons can radiate a fluorophore's structured emission. *Appl. Phys. Lett.* **90**(5), 053107 (2007).
58. C. K. Chen, A. R. B. de Castro, and Y. R. Shen: Surface-Enhanced Second-Harmonic Generation. *Phys. Rev. Lett.* **46**(2), 145 (1981).
59. E. E. Narimanov and A. V Kildishev: Naturally hyperbolic. *Nat. Photonics* **9**, 214 (2015).
60. J. Huang, Z. Qi, L. Li, H. Wang, S. Xue, B. Zhang, X. Zhang, and H. Wang: Self-assembled

vertically aligned Ni nanopillars in CeO2 with anisotropic magnetic and transport properties for energy applications. *Nanoscale* **10**(36), 17182 (2018).

61. J. Huang, L. Li, P. Lu, Z. Qi, X. Sun, X. Zhang, and H. Wang: Self-assembled Co–BaZrO3 nanocomposite thin films with ultra-fine vertically aligned Co nanopillars. *Nanoscale* **9**, 7970 (2017).

62. Q. Su, W. Zhang, P. Lu, S. Fang, F. Khatkhatay, J. Jian, L. Li, and H. Wang: Self-Assembled Magnetic Metallic Nanopillars in Ceramic Matrix with Anisotropic Magnetic and Electrical Transport Properties. *ACS Appl. Mater. Interfaces* **8**, 20283 (2016).

63. X. Sun, Q. Li, J. Huang, M. Fan, B. X. Rutherford, R. L. Paldi, J. Jian, X. Zhang, and H. Wang: Strain-driven nanodumbbell structure and enhanced physical properties in hybrid vertically aligned nanocomposite thin films. *Appl. Mater. Today* **16**, 204 (2019).

64. X. Sun, Q. Li, J. Huang, J. Jian, P. Lu, X. Zhang, J. L. Macmanus-Driscoll, and H. Wang: Strain and property tuning of the 3D framed epitaxial nanocomposite thin films via interlayer thickness variation. *J. Appl. Phys.* **125**(8), 082530 (2019).

65. H. Zheng, F. Straub, Q. Zhan, P. Yang, W. Hsieh, F. Zavaliche, Y. Chu, U. Dahmen, and R. Ramesh: Self-Assembled Growth of BiFeO3 – CoFe2O4 Nanostructures. *Adv. Mater.* **18**, 2747 (2006).

66. F. Khatkhatay, A. Chen, J. H. Lee, W. Zhang, H. Abdel-Raziq, and H. Wang: Ferroelectric properties of vertically aligned nanostructured BaTiO 3-CeO2 thin films and their integration on silicon. *ACS Appl. Mater. Interfaces* **5**(23), 12541 (2013).

67. X. Gao, L. Li, J. Jian, H. Wang, M. Fan, J. Huang, X. Wang, and H. Wang: Vertically Aligned Nanocomposite BaTiO3:YMnO3 Thin Films with Room Temperature Multiferroic Properties toward Nanoscale Memory Devices. *ACS Appl. Nano Mater.* **1**, 2509 (2018).

68. M. Fan, H. Wang, S. Misra, B. Zhang, Z. Qi, X. Sun, J. Huang, and H. Wang: Microstructure, Magnetic, and Magnetoresistance Properties of La0.7Sr0.3MnO3:CuO Nanocomposite Thin Films. *ACS Appl. Mater. Interfaces* **10**, 5779 (2018).

69. Q. Su, W. Zhang, P. Lu, S. Fang, F. Khatkhatay, J. Jian, L. Li, F. Chen, X. Zhang, J. L. MacManus-Driscoll, A. Chen, Q. Jia, and H. Wang: Self-Assembled Magnetic Metallic Nanopillars in Ceramic Matrix with Anisotropic Magnetic and Electrical Transport Properties. *ACS Appl. Mater. Interfaces* **8**, 20283 (2016).

70. S. Zhao, Y. Zhou, K. Zhao, Z. Liu, P. Han, S. Wang, W. Xiang, Z. Chen, H. Lü, B. Cheng, and G. Yang: Violet luminescence emitted from Ag-nanocluster doped ZnO thin films grown on fused quartz substrates by pulsed laser deposition. *Phys. B Condens. Matter* **373**(1), 154 (2006).

71. T. Sasaki, N. Koshizaki, J. W. Yoon, and K. M. Beck: Preparation of Pt/TiO2 nanocomposite thin films by pulsed laser deposition and their photoelectrochemical behaviors. *J. Photochem. Photobiol. A Chem.* **145**(1–2), 11 (2001).

72. Z. Qi, J. Jian, J. Huang, J. Tang, H. Wang, V. G. Pol, and H. Wang: LiNi0.5Mn0.3Co0.2O2/Au nanocomposite thin film cathode with enhanced electrochemical properties. *Nano Energy* **46**, 290 (2018).

73. M. Lee, R. Arras, R. Takahashi, B. Warot-Fonrose, H. Daimon, M. J. Casanove, and M. Lippmaa: Noble Metal Nanocluster Formation in Epitaxial Perovskite Thin Films. *ACS Omega* **3**(2), 2169 (2018).

74. J. Jian, X. Wang, S. Misra, X. Sun, Z. Qi, X. Gao, J. Sun, A. Donohue, D. G. Lin, V. Pol, J. Youngblood, H. Wang, L. Li, J. Huang, and H. Wang: Broad Range Tuning of Phase Transition Property in VO2 Through Metal-Ceramic Nanocomposite Design. *Adv. Funct.*

Mater. **29**, 1903690 (2019).

75. S. Misra, L. Li, J. Jian, J. Huang, X. Wang, D. Zemlyanov, J. Jang, F. H. Ribeiro, and H. Wang: Tailorable Au Nanoparticles Embedded in Epitaxial TiO 2 Thin Films for Tunable Optical Properties. *ACS Appl. Mater. Interfaces* **10** (2018).

76. M. Jakob, H. Levanon, and P. V. Kamat: Charge distribution between UV-irradiated TiO2 and gold nanoparticles: Determination of shift in the Fermi level. *Nano Lett.* **3**(3), 353 (2003).

77. S. Peters, S. Peredkov, M. Neeb, W. Eberhardt, and M. Al-Hada: Size-dependent XPS spectra of small supported Au-clusters. *Surf. Sci.* **608**, 129 (2013).

78. Z. Qi, J. Tang, S. Misra, C. Fan, P. Lu, J. Jian, Z. He, V. G. Pol, X. Zhang, and H. Wang: Enhancing electrochemical performance of thin film lithium ion battery via introducing tilted metal nanopillars as effective current collectors. *Nano Energy* **69**, 104381 (2020).

79. D. Zhang, S. Misra, L. Li, X. Wang, J. Jian, P. Lu, X. Gao, X. Sun, Z. Qi, M. Kalaswad, X. Zhang, and H. Wang: Tunable Optical Properties in Self-Assembled Oxide-Metal Hybrid Thin Films via Au-Phase Geometry Control: From Nanopillars to Nanodisks. *Adv. Opt. Mater.* **8**, 1901359 (2019).

80. J. Huang, J. L. Macmanus-driscoll, and H. Wang: New epitaxy paradigm in epitaxial self-assembled oxide vertically aligned nanocomposite thin films. *J. Mater. Res.* **32**(21), 4054 (2017).

81. B. Zhang, J. Huang, B. X. Rutherford, P. Lu, S. Misra, M. Kalaswad, Z. He, X. Gao, X. Sun, L. Li, and H. Wang: Tunable, room-temperature multiferroic Fe-BaTiO3 vertically aligned nanocomposites with perpendicular magnetic anisotropy. *Mater. Today Nano* **11** (2020).

82. B. Zhang, M. Fan, L. Li, J. Jian, J. Huang, H. Wang, M. Kalaswad, and H. Wang: Tunable magnetic anisotropy of self-assembled Fe nanostructures. *Appl. Phys. Lett.* **112**, 013104 (2018).

83. H. L. Skriver and N. M. Rosengaard: Surface energy and work function of elemental metals. *Phys. Rev. B* **46**(11), 7157 (1992).

84. X. Weng, M. Hennes, A. Coati, A. Vlad, Y. Garreau, M. Sauvage-Simkin, E. Fonda, G. Patriarche, D. Demaille, F. Vidal, and Y. Zheng: Ultrathin Ni nanowires embedded in SrTiO3: Vertical epitaxy, strain relaxation mechanisms, and solid-state amorphization. *Phys. Rev. Mater.* **2**(10), 106003 (2018).

85. F. Vidal, Y. Zheng, P. Schio, F. J. Bonilla, M. Barturen, J. Milano, D. Demaille, E. Fonda, A. J. A. De Oliveira, and V. H. Etgens: Mechanism of localization of the magnetization reversal in 3 nm wide Co nanowires. *Phys. Rev. Lett.* **109**(11), 117205 (2012).

86. K. Ikemiya, Y. Hirose, and T. Hasegawa: Fabrication and magnetic properties of fcc-Co nanorods embedded in epitaxial thin films of anatase TiO2 as a transparent matrix. *J. Phys. Chem. C* **115**(5), 1776 (2011).

87. F. J. Bonilla, A. Novikova, F. Vidal, Y. Zheng, E. Fonda, D. Demaille, V. Schuler, A. Coati, A. Vlad, Y. Garreau, M. Sauvage Simkin, Y. Dumont, S. Hidki, and V. Etgens: Combinatorial growth and anisotropy control of self-assembled epitaxial ultrathin alloy nanowires. *ACS Nano* **7**(5), 4022 (2013).

88. B. Zhang, J. Huang, J. Jian, B. X. Rutherford, L. Li, S. Misra, X. Sun, and H. Wang: Tuning magnetic anisotropy in Co-BaZrO3 vertically aligned nanocomposites for memory device integration. *Nanoscale Adv.* **1**(11), 4450 (2019).

89. F. Vidal, Y. Zheng, J. Milano, D. Demaille, P. Schio, E. Fonda, and B. Vodungbo:

Nanowires formation and the origin of ferromagnetism in a diluted magnetic oxide. *Appl. Phys. Lett.* **95**(15), 93 (2009).

90. B. Zhang, J. Huang, B. Rutherford, P. Lu, S. Misra, M. Kalaswad, Z. He, X. Gao, X. Sun, L. Li, and H. Wang: Tunable room temperature multiferroic Fe-BaTiO3 vertically aligned nanocomposite with perpendicular magnetic anisotropy. *Mater. Today Nano* **11**, 100083 (2020).

91. C. Zhang, D. H. Kim, X. Huang, X. Y. Sun, N. M. Aimon, S. J. Chua, and C. A. Ross: Magnetic and Photoluminescent Coupling in SrTi0.87Fe0.13O3-I/ZnO Vertical Nanocomposite Films. *ACS Appl. Mater. Interfaces* **9**(37), 32359 (2017).

92. Y. J. Zeng, N. Gauquelin, D. Y. Li, S. C. Ruan, H. P. He, R. Egoavil, Z. Z. Ye, J. Verbeeck, J. Hadermann, M. J. Van Bael, and C. Van Haesendonck: Co-Rich ZnCoO Nanoparticles Embedded in Wurtzite Zn1-xCoxO Thin Films: Possible Origin of Superconductivity. *ACS Appl. Mater. Interfaces* **7**(40), 22166 (2015).

93. C. O. Amorim, F. Figueiras, J. S. Amaral, P. M. Vaghefi, P. B. Tavares, M. R. Correia, A. Baghizadeh, E. Alves, J. Rocha, and V. S. Amaral: Peculiar Magnetoelectric Coupling in BaTiO3:Fe113 ppm Nanoscopic Segregations. *ACS Appl. Mater. Interfaces* **7**(44), 24741 (2015).

94. H. Li, C. Wang, D. Li, P. Homm, M. Menghini, J. P. Locquet, C. Van Haesendonck, M. J. Van Bael, S. Ruan, and Y. J. Zeng: Magnetic orders and origin of exchange bias in Co clusters embedded oxide nanocomposite films. *J. Phys. Condens. Matter* **31**, 155301 (2019).

95. B. Zhang, M. Kalaswad, B. X. Rutherford, S. Misra, Z. He, H. Wang, Z. Qi, A. E. Wissel, X. Xu, and H. Wang: Au-Encapsulated Fe Nanorods in Oxide Matrix with Tunable Magneto-Optic Coupling Properties. *ACS Appl. Mater. Interfaces* In Press (2020),

https://doi.org/10.1021/acsami.0c14424.

96. M. Kalaswad, D. Zhang, X. Gao, L. L. Contreras, H. Wang, X. Wang, and H. Wang: Integration of Hybrid Plasmonic Au-BaTiO3 Metamaterial on Silicon Substrates. *ACS Appl. Mater. Interfaces* **11**(48), 45199 (2019).